Sessa, M. F. and R. J. Trapp, 2023: Environmental and radar-derived predictors of tornado intensity within ongoing convective storms. *J. Operational Meteor.,* **11** (5), 49–71, doi: https://doi.org/10.15191/nwajom.2023.1105.

Environmental and Radar-Derived Predictors of Tornado Intensity within Ongoing Convective Storms

MICHAEL F. SESSA and ROBERT J. TRAPP
Department of Atmospheric Sciences, University of Illinois, Urbana, Illinois

(Manuscript received 20 March 2022; review completed 15 February 2023)

ABSTRACT

Analyses of Doppler radar data and environmental parameters for 300 tornado cases are used to propose an alternative framework for tornado intensity prediction during pretornadic stages of ongoing storms, conditional on tornadogenesis. This framework is founded on the robust relationship (R^2 = 0.69) between pretornadic mesocyclone width and the EF rating of the subsequent tornado. In contrast, the linear relationship between pretornadic mesocyclone intensity and EF scale is much weaker (R^2 = 0.29). Environmental information for each case was additionally used to explore relationships between environmental parameters and tornado intensity. Such relationships depend in part on how the tornado-intensity categories are distributed [i.e., nonsignificant (EF0–1) versus significant (EF2–5), or weak (EF0–1) versus strong (EF2–3) versus violent (EF4–5)]. Low-level shear parameters discriminate the environments of significant tornadoes from nonsignificant tornadoes, but not the environments of violent tornadoes from strong tornadoes. The converse is true for thermodynamic parameters. Operational implementation of this framework for the purposes of impact-based warnings will require real-time, automated quantification of mesocyclone width in addition to intensity and other attributes. The information gained from the pretornadic analysis demonstrated in this study would allow an operational forecaster to be aware of—and communicate—information about potential tornado intensity in warning text to the public before a tornado develops to better protect life and property. Currently, these relationships are being utilized in machine learning models for binary prediction of non-significant versus significant tornado intensity where skill is being demonstrated.

1. Introduction

It is well documented that strong to violent tornadoes cause a disproportionate amount of damage and fatalities (Ashley 2007; Simmons and Sutter 2011; Anderson-Frey and Brooks 2019). Implied by this statement is the need for robust operational tools that focus on *tornado intensity* rather than simply on *tornadogenesis*, especially given that most tornadoes are nonsignificant (EF0–EF1; Brooks et al. 2003). Toward this end, there have been efforts to develop methods to *diagnose the intensity of an ongoing tornado*. As first successfully demonstrated by Toth et al. (2013), these methods primarily involve the use of radar-based characteristics of the tornadic circulation and parent storm (also see Kingfield and LaDue 2015; Gibbs 2016; Thompson et al. 2017; Van Den Broeke 2017; Smith et al. 2015, 2020a), which also can be coupled to the use of environmental parameters (e.g., Cohen et al. 2018), such as the supercell composite parameter (SCP) and significant tornado parameter (STP; e.g., Thompson et al. 2012). Reiterating, these methods require the existence of a tornado, and thus their applications are conditional on tornadogenesis [Thompson et al. (2017) also included null cases in their analysis].

There have been fewer efforts to develop methods to *predict tornado intensity during pretornadic stages of ongoing storms*. These appear to include the following: (i) Gibbs (2016) and Gibbs and Bowers (2019), who found that the depth, rotational velocity, and temporal evolution of the width and rotational velocity of pretornadic mesocyclones had operationally useful skill in differentiating between either significantly tornadic, weakly tornadic, or nontornadic supercells, (ii) Marion et al. (2019), who used satellite-diagnosed overshooting-top area (OTA) to gauge potential tornado intensity, (iii) Sessa and Trapp (2020;

Corresponding author address: Michael F. Sessa, Department of Atmospheric Sciences, 1301 West Green Street, Urbana, IL 61801
E-mail: msessa2@illinois.edu

hereinafter ST20), who demonstrated that pretornadic mesocyclone width (differential velocity) was strongly (only moderately) correlated to tornado intensity, (iv) Baerg et al. (2020), who used the characteristics of the lifetime of pretornadic circulations at the 0.5° radar elevation angle combined with the STP to produce tornado probabilities preceding tornadogenesis, and found a more substantial increase in tornado probabilities in the 15 min preceding tornadogenesis for significant tornadoes (EF2+) than for non-significant tornadoes (EF0–1), and (v) most recently, French and Kingfield (2021) who found, using differential reflectivity (Z_{DR}) as a proxy for midlevel updraft area and strength, that stronger tornadoes tended to have a larger Z_{DR} column area at the time of tornadogenesis than did weaker tornadoes and nontornadic supercells at their time of peak 0–1-km azimuthal shear.

The studies by Marion et al. (2019), ST20, and French and Kingfield (2021) all provide observational support of the Trapp et al. (2017) hypothesis that intense tornadoes should form more readily out of wide, rotating updrafts. For reference, the simplistic theoretical underpinning of this hypothesis is conservation of angular momentum (or, equivalently vortex stretching); a more complicated dynamical pathway linking updraft area to downdraft area to baroclinically generated horizontal vorticity to near-ground vertical vorticity is described by Trapp et al. (2017; also see Marion and Trapp 2019). The results of these studies may seem inconsistent with the pervading guidance relating "clear and tight circulations" to significant tornadoes (e.g., Thompson et al. 2017; Smith et al. 2020a). This guidance, incidentally, also is based fundamentally on angular-momentum-conservation or vortex-stretching concepts. However, the clear and tight characterization applies specifically to the circulation associated with an *ongoing* tornado [i.e., a circulation that simultaneously represents the tornado and, in most cases, its parent, mesocyclonic vortex; see section 2c of Smith et al. (2015)]. In contrast, the "wide-mesocyclone–significant-tornado" relationship revealed by ST20 applies to *pretornadic* circulations. Such a pretornadic focus eliminates the effects of the tornado itself on the mesocyclone characteristics and, most importantly, allows for the development of tools for tornado-intensity prediction conditional on tornadogenesis, rather than for tornado-intensity diagnosis conditional on tornadogenesis.

Herein we use an expanded dataset to provide further evidence of the robust relationship between tornado intensity and pretornadic mesocyclone width. This relationship is shown to hold equally well for pretornadic mesocyclones quantified at heights <1 km and at heights extending to ~2 km. We also use environmental information for each of the cases in this dataset to explore relationships between environmental parameters and tornado intensity. We show that such relationships depend in part on how the tornado-intensity categories are distributed. For example, low-level shear parameters discriminate the environments of significant tornadoes from nonsignificant tornadoes, but not the environments of violent (EF4–5) tornadoes from strong (EF2–3) tornadoes. The converse is true for thermodynamic parameters. Finally, we discuss how our results can be implemented in an operational setting. This includes the use of machine learning for binary, tornado intensity prediction.

2. Data and methods

a. Development of radar-based dataset

ST20 assembled an observational radar dataset of 102 tornado cases that encompassed a reasonable sample of parent-storm morphologies, seasonal and geographical diversity, and variations in environmental conditions. For the purposes of the current study and its companion (e.g., Sessa and Trapp 2022), the dataset was expanded to 300 tornado cases primarily from 2019 and 2020 (Fig. 1). Cases were selected using the NCEI Storm Events Database (https://www.ncdc.noaa.gov/stormevents/). The basic case-selection methods of ST20 were employed. Summarizing, it was required that all tornadoes were within ≤100 km of a WSR-88D, to lessen the impact of radar range and beam width limitations (e.g., Wood and Brown 1997). In addition, each tornado had to be the first produced by its respective parent storm. This restriction was imposed to avoid potential confusion about how to classify a mesocyclone as pretornadic when in the presence of ongoing/dissipated tornadoes; it is demonstrated below, however, that the overall conclusions of the study should be insensitive to this restriction. Finally, no tornado within 1 h and 80 km of another tornado was included in the dataset if its EF rating was more than one EF category lower than the peak EF rating within this time and space range. This was to ensure the strongest tornadoes within a particular environment were sampled without leading to the removal of too many cases from this condition. The expanded dataset

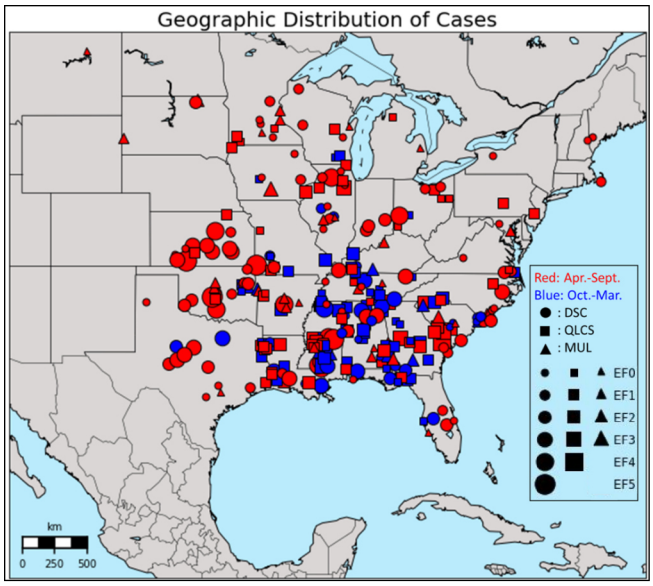

Figure 1. Geographic distribution of the 300-case dataset (April 2011–October 2020), also showing convective mode [circles: Discrete cases (DSC), squares: Quasi-linear convective system cases (QLCS), triangles: Multicell cases (MUL)], tornado intensity (increasing intensity with increasing shape size), and season (red: warm or blue: cool). *Click image for an external version; this applies to all figures and animations hereafter.*

is composed of the following: 78 EF0s, 116 EF1s, 59 EF2s, 33 EF3s, 10 EF4s, and 4 EF5s, which generally reflects the overall climatological distribution (Brooks et al. 2003). The relatively smaller number of EF0s was due to the tendency for insufficient pretornadic radar sampling of such events [i.e., weak tornadoes often formed and then dissipated within one or two radar volume scans and thus were not preceded by a time- and space-resolvable pretornadic circulation (especially for the cases farthest from the radar)]. The difficulty in applying this technique to the weaker, more diffuse circulations that tend to precede EF0 tornadoes is a limitation, but the information provided by these cases with short-lived pretornadic circulations is still important to include because it is relevant in a real-time operational setting. Additionally, if a storm contains a poorly resolved, weak, diffuse mesocyclone, it should be intuitive that the storm has a very low probability of producing a significant tornado if any tornado at all, and this also highlights the operational difficulty of identifying the weaker rotation signatures that may precede weak tornadoes (especially for quasi-linear convective system cases and storms that are a greater distance from the radar).

The Gibson Ridge radar software (GR2Analyst) was used to manually analyze single-site, WSR-88D level II data for each case. Reflectivity criteria (see ST20, and references therein) were employed to categorize the convective mode of the parent storm of each tornado. Of the 300 cases in the dataset, 130 were associated with discrete supercells (DSC), 124 with quasi-linear convective systems (QLCS), and 46 with clusters or multicells (MUL). As explained in more detail in ST20, Doppler velocity data were then used to quantify the pretornadic mesocyclone width, defined here as the linear distance between the inbound and outbound velocity peaks in the vortex couplet, as well as the pretornadic mesocyclone intensity, equated here to the differential velocity (ΔV) computed using the inbound and outbound velocity peaks. From ST20 [methods similar to Smith et al. (2012)], the presence of a mesocyclone required a peak $\Delta V \geq 10$ m s^{-1} over a horizontal distance of <7 km, over the depth of the three lowest radar elevation angles, during at least one volume scan. The pretornadic mesocyclone metrics (Table 1) were evaluated at the three lowest radar-elevation angles, for up to four volume scans during the lifetime of the identifiable mesocyclone, through the volume scan just prior to the time of reported tornadogenesis. To clarify, at least one pretornadic volume scan was required. There were mesocyclones in the dataset that had pretornadic lifetimes exceeding four volume scans, and although there were consistent results when a greater number of scans were included (when present), analysis of characteristics beyond four volume scans did not provide unique information. This was done to attain a representative measure of the mesocyclone and its evolution without having unnecessary data collection. The percentages of cases in which four, three, two, and one volume scan were used in their analysis are 56%, 21%, 19%, and 4%, respectively.

Before including a case, the quality of the velocity data was thoroughly considered to ensure the maximum inbound and outbound velocities were associated with a mesocyclone. When contaminants such as three body scatter spikes and dealiasing issues prevented a mesocyclone from being resolved, the case was not used. Additionally, to further ensure that the velocity maxima were associated with a rotating updraft instead of divergence or convergence signatures the positioning of the extrema with respect to one another and the larger

Table 1. List of pretornadic, radar-based parameters analyzed.

Parameter	Description
Total average pretornadic mesocyclone width (km)	The mean mesocyclone width over the lowest three elevation angles and all volume scans analyzed during the pretornadic period.
Peak pretornadic mesocyclone intensity (ΔV, m s^{-1})	The maximum ΔV over the lowest three elevation angles and all volume scans analyzed during the pretornadic period.
Distance from radar (km)	The distance from the radar to the approximate location of the tornado at the time of tornadogenesis using the 0.5° elevation angle scan closest to the time of tornadogenesis.
Convective mode	Either discrete supercell, QLCS, or multicell [see Sessa and Trapp (2020) for further description]

storm structure from reflectivity data were considered. Based on the analyses presented by Wood and Brown (1997), the potential errors in mesocyclone width at radar ranges ≤100 km appear to be ≤500 m, and the potential errors in mesocyclone intensity within these same ranges are ≤3 m s^{-1}. While these are potential sources of inconsistencies in the radar analyses, the larger sample size of events studied should represent the spread of error that is inherent in radar studies, and there is consistency between the methods here and operational practice as these radar range and beam width discrepancies (e.g., averaging velocities across a beam width, separation of circulation center from center of beam) would be present in real-time radar assessments as well.

We acknowledge that there are other mesocyclone metrics that could have been considered, including mesocyclone depth, mesocyclone width and intensity over more than the lowest three elevation angles, and the temporal evolution of width, depth, and intensity (Gibbs 2016; Gibbs and Bowers 2019). Characteristics in polarimetric variables such as Z_{DR} columns and arcs also could have been considered (Van Den Broeke 2017, 2020; French and Kingfield 2021). However, pretornadic mesocyclone width and intensity most directly relate to the Trapp et al. (2017) hypothesis on tornado intensity, and therefore are the characteristics of focus herein. Indeed, as will be shown, mesocyclone width is a robust predictor of tornado intensity for the cases in this expanded dataset.

Although we have no specific hypothesis linking mesocyclone width and/or intensity to tornadogenesis, there may be utility in exploring the analyzed mesocyclone characteristics in relation to tornadogenesis through the inclusion of a small sample of nontornadic or null cases. Herein, nontornadic storms were defined as storms that were tornado-warned by the National Weather Service but did not produce a reported tornado. The analysis reference time (T-0) was the time of the first tornado warning issued for a non-tornado producing storm; thus, T-0 is meant to correspond to the time of tornadogenesis failure, as originally introduced by Trapp (1999). Only storms with one circulation within the warning box were included (e.g., QLCS cases with large warning boxes including multiple circulations were excluded). The Iowa Environmental Mesonet storm warning database was used to identify tornado warnings that were the first to be issued for a particular storm. The Storm Prediction Center (SPC) severe weather events archive (https://www.spc.noaa.gov/exper/archive/event.php?date=20211210) as well as the NCEI Storm Events Database (https://www.ncdc.noaa.gov/stormevents/) were used to confirm that a particular storm and associated mesocyclone never produced a tornado. If this basic criterion was met, then radar data were analyzed to confirm that the case met the other criteria outlined above (e.g., within 100 km of a radar, presence of a mesocyclone over the lowest three radar elevation angles). The mesocyclone characteristics over the pre-warning time were then analyzed following the same methods applied to tornadic storms. Cases were selected from the previous two years and are seasonally and geographically diverse. As will be discussed, the mesocyclone widths and intensities of our 35 nontornadic cases are distinguishable from those associated with EF3+ tornadic cases, but not from weaker tornadic cases.

b. Development of environmental dataset

There are numerous factors to consider when evaluating near-storm, pretornadic environmental conditions (e.g., Brooks et al. 1994; Thompson et al. 2003; Potvin et al. 2010, Coniglio 2012; Parker 2014; Smith et al. 2015), such as how to sample the environment (e.g., proximity, inflow or pre-/ongoing/post-convective environments) and what time and space scales are most appropriate. For example, Potvin et al. (2010) found using a large dataset of observed

proximity soundings associated with significant tornado reports that there appears to be a favorable spatiotemporal distance from a thunderstorm-related event that it is close enough to capture the background environment of the storm while being far enough away to minimize impacts of a storm's influence on the local environment (often referred to as convective feedbacks). This optimum spatiotemporal distance was found to be within 40–80 km and 1–2 h of the storm or event, and several studies have adopted these guidelines (e.g., Coniglio 2012; Reames 2017; Coniglio and Parker 2020), although only one sounding was used for each storm and only differences in distance, not azimuth, were considered.

One issue with rawinsonde datasets is that they often lack adequate spatial and temporal coverage. Model-based soundings have high spatial and temporal resolution, but also have model biases and inaccuracies, dependences on model parameterizations, and potential convective feedbacks that can result in errors in model soundings as compared to observed soundings in a pre-convective environment (Thompson et al. 2003; Coniglio 2012; Laflin 2013). Even with these limitations, previous studies have concluded that model analysis soundings provide a reasonable proxy for observed soundings in severe thunderstorm environments, and that certain sounding parameters have skill in identifying supercell and tornado environments, especially when using 0- and 1-h analysis data (Markowski et al. 2003; Thompson et al. 2003; King and Kennedy 2019).

Model soundings from the Rapid Update Cycle (Benjamin et al. 2004) and the Rapid Refresh (Benjamin et al. 2016) have been used in studies of supercell and severe thunderstorm environments. Several studies have sampled the environment from the nearest analysis grid point at the closest hour prior to a significant severe event (Markowski et al. 2003; Thompson et al. 2003, 2007; Grams et al. 2012; Brotzge et al. 2013; Nowotarski and Jensen 2013). Others have sampled the environment at the grid point of maximum STP within a warning area or a certain distance to the storm (Smith et al. 2015; Anderson-Frey et al. 2016). To increase the representativeness of surface conditions, some studies combined the model analyses with objectively analyzed surface observations (Thompson et al. 2007; Coniglio 2012; Grams et al. 2012; Thompson et al. 2012).

Guided and motivated by the previously described studies, the 13-km Rapid Refresh Version 3 (RAP) analysis data from the THREDDS database (https://www.ncei.noaa.gov/access/thredds-user-guide) were used herein. Beginning with the 3D state variables from the RAP analysis, 42 desired environmental variables (Table 2) were computed either manually or using the Unidata MetPy python module (May et al. 2022). The RAP analysis time nearest but prior to the time of tornadogenesis was used for the computations. For example, if tornadogenesis for a particular case took place at 2132 UTC, then the 2100 UTC RAP analysis hour was used. This choice of analysis time was based on experimentation, as was the choice of an analysis domain with horizontal dimensions 130 km × 130 km, centered on the RAP grid point closest to the location of tornadogenesis. The domain was not centered on the grid point closest to the greatest EF rating because we cannot assume reliable spatial coverage of damage indicators along a tornado path, nor can we assume that EF ratings would be continuous along a given damage path even with an abundance of damage indicators. To limit the impacts of convective feedbacks (or so-called convective contamination), any grid point with a 1-km AGL simulated reflectivity >20 dBZ was excluded from the sampling domain. Additionally, any grid point with a most-unstable (MU) convective available potential energy (MUCAPE) <75 J kg^{-1} was excluded. This threshold was chosen after sensitivity tests were completed using different thresholds with cases where a cold front or warm front dissected the sampling box. Thus, this successfully acted to remove grid points from behind cold fronts or ahead of warm fronts without removing grid points that represented the near-storm environment. Last, values of sampled parameters ≤0 were excluded. These criteria reduced the number of grid-point values in the sampling domain and therefore varied the number of grid-point values from case to case.

The maximum, mean, and median value of each parameter in the 130 km × 130 km sampling domain were calculated across cases, as was the standard deviation, to understand how each parameter varied across the sampling domains. Based on intercomparisons across several cases, the mean value in the sampling domain was chosen for the analyses presented in section 3. This allowed for the near-storm environment to be represented by multiple grid points rather than by only one (i.e., the maximum value, or value closest to the location of tornadogenesis). Because the focus of this analysis is on relationships between the near-storm environment and tornado

Table 2. List of pretornadic environmental parameters computed.

Parameter	Description
100-mb Mixed-Layer Convective Available Potential Energy (MLCAPE, J kg^{-1})	Calculated in MetPy
100-mb Mixed-Layer Convective Inhibition (MLCIN, J kg^{-1})	Calculated in MetPy
Surface-based Convective Available Potential Energy (SBCAPE, J kg^{-1})	Calculated in MetPy
Surface-based Convective Inhibition (SBCIN, J kg^{-1})	Calculated in MetPy
Most-Unstable Convective Available Potential Energy (MUCAPE, J kg^{-1})	Calculated in MetPy
Most-Unstable Convective Inhibition (MUCIN, J kg^{-1})	Calculated in MetPy
0–3-km Convective Available Potential Energy (CAPE03, J kg^{-1})	Calculated in MetPy using layer interpolation
Lifted Index (LI, °C)	Calculated in MetPy
0–8-km Bulk Shear (S08, m s^{-1})	Calculated in MetPy using layer interpolation
0–6-km Bulk Shear (S06, m s^{-1})	Calculated in MetPy using layer interpolation
0–3-km Bulk Shear (S03, m s^{-1})	Calculated in MetPy using layer interpolation
0–1-km Bulk Shear (S01, m s^{-1})	Calculated in MetPy using layer interpolation
0–500-m bulk shear (S500, m s^{-1})	Calculated in MetPy using layer interpolation
Effective bulk shear (EBS, m s^{-1})	Manually calculated using methods and equations outlined in Thompson et al. (2007)
Bunkers Right Storm Motion (BR, m s^{-1})	Calculated in MetPy
0–6-km Mean Flow (06Mean, m s^{-1})	Calculated in MetPy
0–1-km Storm Relative Helicity (01SRH, m^2 s^{-2})	Calculated in MetPy
0–3-km Storm Relative Helicity (03SRH, m^2 s^{-2})	Calculated in MetPy
0–500-m Storm Relative Helicity (0500SRH, m^2 s^{-2})	RAP analysis variable
Effective Storm Relative Helicity (ESRH, m^2 s^{-2})	Manually calculated using methods and equations outlined in Thompson et al. (2007)
Effective Layer Base Height (ELB, m)	Manually calculated using methods and equations outlined in Thompson et al. (2007)
Effective Layer Top Height (ELT, m)	Manually calculated using methods and equations outlined in Thompson et al. (2007)
Effective Layer Depth (ELD, m)	Manually calculated using methods and equations outlined in Thompson et al. (2007)
0–2-km Storm Relative Wind (02SRW, m s^{-1})	Manually calculated using MetPy layer interpolation
4–6-km Storm Relative Wind (46SRW, m s^{-1})	Manually calculated using MetPy layer interpolation
9–11-km Storm Relative Wind (911SRW, m s^{-1})	Manually calculated using MetPy layer interpolation
0–3-km Lapse Rate (03LR, °C km^{-1})	Manually calculated using MetPy layer interpolation
3–6-km Lapse Rate (36LR, °C km^{-1})	Manually calculated using MetPy layer interpolation
Lifting Condensation Level Height (LCLh, m)	Calculated in MetPy
Level of Free Convection Height (LFCh, m)	Calculated in MetPy
Lifting Condensation Level to Level of Free Convection Height Difference (LCL-LFC, m)	Manually calculated
0–3-km Relative Humidity (03RH, %)	Calculated in MetPy using layer interpolation
3–6-km Relative Humidity (36RH, %)	Calculated in MetPy using layer interpolation
Lifting Condensation Level to Level of Free Convection Relative Humidity (LCL-LFC-RH, %)	Manually calculated
0–1-km Energy Helicity Index (01EHI)	Manually calculated using methods and equations outlined in Thompson et al. (2003)
0–3-km Energy Helicity Index (03EHI)	Manually calculated using methods and equations outlined in Thompson et al. (2003)
Fixed-layer Supercell Composite Parameter (SCPf)	Manually calculated using methods and equations outlined in Thompson et al. (2003)
Effective-layer Supercell Composite Parameter (SCPe)	Calculated in MetPy
Fixed-layer Significant Tornado Parameter (STPf)	Calculated in MetPy
Violent Tornado Parameter (VTP)	Manually calculated using methods and equations outlined in Hampshire et al. (2018)
0–1-km Tornadic Energy Helicity Index (torEHI)	Manually calculated using methods and equations outlined from SPC
Tornadic Tilting and Stretching Parameter (TTS)	Manually calculated using methods and equations outlined from the SPC
Critical Angle (CA, degrees)	Calculated in MetPy

intensity, considering a larger area that the storm and tornado may experience is particularly relevant.

3. Analysis

a. Pretornadic characteristics of mesocyclones associated with significant versus nonsignificant tornadoes

The box-and-whisker plot in Fig. 2a confirms the robust relationship found by ST20 between pretornadic mesocyclone width and the EF of the resultant tornado. In the linear regression between pretornadic mesocyclone width and EF scale, the coefficient of determination (R^2) is 0.69 (Fig. 2b), which supports the remarkably clear separation shown in Fig. 2a for the widths associated with lower-end (EF0–1) versus higher-end (EF3–5) tornadoes. A tabular view of this separation of mean pretornadic mesocyclone width is provided in Tables 3 and 4. The same R^2 results from a linear regression between pretornadic width and estimated tornado windspeeds (not shown). If the EF0–1 tornadoes are omitted from the linear regression, the resultant R^2 is 0.68, which shows that this relationship is robust over the range of significant (EF2+) tornadoes. As a function of convective mode, the widths of

Table 3. Mean and standard deviation of the mean pretornadic mesocyclone width, peak pretornadic mesocyclone ΔV, and spatial mean of each environmental parameter across all cases, separated by non-significant (EF0–1) and significant (EF2–5) tornado intensity.

Parameter	EF0 to EF1 (194 cases)	EF2 to EF5 (106 cases)
Pretornadic Mesocyclone Width (km)	2.04, 0.37	3.28, 0.98
Pretornadic Mesocyclone ΔV (m s^{-1})	35.8, 10.2	47.4, 12.7
100-mb Mixed-Layer Convective Available Potential Energy (MLCAPE, J kg^{-1})	985, 249	1241, 270
100-mb Mixed-Layer Convective Inhibition (MLCIN, J kg^{-1})	–49, 23	–54, 26
Surface-based Convective Available Potential Energy (SBCAPE, J kg^{-1})	1317, 416	1485, 391
Surface-based Convective Inhibition (SBCIN, J kg^{-1})	–63, 34	–60, 29
Most-Unstable Convective Available Potential Energy (MUCAPE, J kg^{-1})	1538, 356	1748, 349
Most-Unstable Convective Inhibition (MUCIN, J kg^{-1})	–20, 16	–23, 16
0–3-km Convective Available Potential Energy (CAPE03, J kg^{-1})	54, 24	52, 22
Lifted Index (LI, °C)	–2.69, 0.91	–2.62, 0.93
0–8-km Bulk Shear (S08, m s^{-1})	25, 2	29, 2.3
0–6-km Bulk Shear (S06, m s^{-1})	23, 1.8	27, 2.0
0–3-km Bulk Shear (S03, m s^{-1})	18, 1.9	22, 1.9
0–1-km Bulk Shear (S01, m s^{-1})	13, 1.6	17, 1.7
0–500-m bulk shear (S500, m s^{-1})	10, 1.4	12, 1.4
Effective bulk shear (EBS, m s^{-1})	21, 2.3	26, 2.2
Bunkers Right Storm Motion (BR, m s^{-1})	15, 1.3	18, 1.2
0–6-km Mean Flow (06Mean, m s^{-1})	18, 1.1	22, 1.1
0–1-km Storm Relative Helicity (01SRH, m^2 s^{-2})	204, 37	274, 43
0–3-km Storm Relative Helicity (03SRH, m^2 s^{-2})	279, 48	372, 58
0–500-m Storm Relative Helicity (0500SRH, m^2 s^{-2})	184, 38	225, 41
Effective Storm Relative Helicity (ESRH, m^2 s^{-2})	196, 54	291, 67
Effective Layer Top Height (ELT, m)	1528, 478	1719, 512
Effective Layer Depth (ELD, m)	1510, 414	1713, 463
0–2-km Storm Relative Wind (02SRW, m s^{-1})	10, 0.63	11, 0.74
4–6-km Storm Relative Wind (46SRW, m s^{-1})	10, 0.82	10, 0.88
9–11-km Storm Relative Wind (911SRW, m s^{-1})	16.3, 2.0	17, 2.3
0–3-km Lapse Rate (03LR, °C km^{-1})	5.72, 0.38	5.82, 0.35
3–6-km Lapse Rate (36LR, °C km^{-1})	6.21, 0.21	6.56, 0.23
Lifting Condensation Level Height (LCLh, m)	389, 126	434, 133
Level of Free Convection Height (LFCh, m)	1707, 760	1916, 786
Lifting Condensation Level to Level of Free Convection Height Difference (LCL-LFC, m)	1401, 815	1559, 764
0–3-km Relative Humidity (03RH, %)	80, 4.5	79, 4.9
3–6-km Relative Humidity (36RH, %)	65, 8.4	59, 8.5
Lifting Condensation Level to Level of Free Convection Relative Humidity (LCL-LFC-RH, %)	83, 5.4	82.5, 6.45
0–1-km Energy Helicity Index (01EHI)	1.01, 0.34	1.84, 0.48
0–3-km Energy Helicity Index (03EHI)	1.51, 0.46	2.61, 0.65
Fixed-layer Supercell Composite Parameter (SCPf)	2.07, 0.51	4.19, 0.98
Effective-layer Supercell Composite Parameter (SCPe)	4.96, 1.77	9.18, 2.59
Fixed-layer Significant Tornado Parameter (STPf)	1.27, 0.51	2.46, 0.86
Violent Tornado Parameter (VTP)	0.89, 0.42	2.01, 0.88
0–1-km Tornadic Energy Helicity Index (torEHI)	0.62, 0.29	1.68, 0.64
Tornadic Tilting and Stretching Parameter (TTS)	1.65, 0.77	2.9, 1.21
Critical Angle (CA, degrees)	67, 11	63, 8.5

supercell mesocyclones exhibit higher correlations to EF (R^2 = 0.77) than do the widths of QLCS mesocyclones/mesovortices (R^2 = 0.48).

Specifically shown in Fig. 2a are widths that are averaged in height over the three lowest radar scans, and in time over the pretornadic (or pre-warning) volume scans (see Table 1); ST20 demonstrated, however, that this relationship can be generalized to widths at individual scans (e.g., the lowest) and at individual pretornadic times. Indeed, there is relatively little time variability in the pretornadic width, such that, except for the few minutes immediately prior to tornadogenesis when mesocyclone contraction occurs, a wide (narrow) mesocyclone is consistently wide (narrow) (Fig. 3; also see ST20) allowing for these characteristics to be more easily used in a prognostic manner. Our results do show that the majority of EF3 and greater rated tornadoes (which tended to be

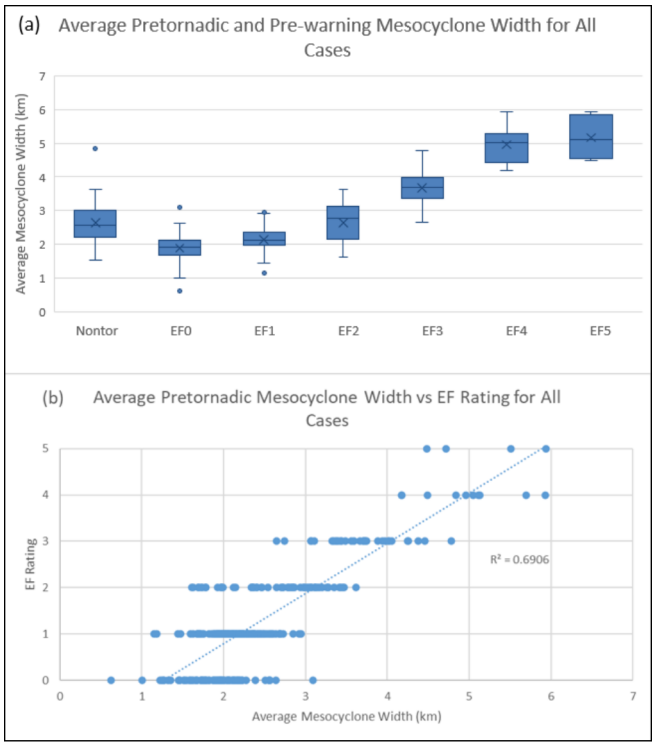

Figure 2. (a) Box-and-whiskers plot of the total average pretornadic mesocyclone width (km) of EF0–5 tornadoes and the total average pre-warning mesocyclone width (km) of nontornadic storms for all cases. (b) Scatterplot of the relationship between the total average pretornadic mesocyclone width (km) and the EF rating of the resultant tornado for all cases. In (a), the mean is represented by the "X" and the median by the bar. The top and bottom of the box represent the 3rd and 1st quartiles with exclusive medians, respectively. The top whisker represents the boundary of 1.5 times the interquartile range above the 3rd quartile, and the bottom whisker represents the boundary of 1.5 times the interquartile range below the 1st quartile. Any point beyond these whiskers is plotted as an outlier point.

preceded by wider pretornadic circulations) were associated with mesocyclones that narrowed and strengthened just prior to tornadogenesis. This supports the idea that a pretornadic mesocyclone that shows an increase in ΔV and a decrease in width immediately prior to tornadogenesis may be more likely to produce a tornado, specifically a potentially strong tornado, and this pattern has been found in other observational studies as well (e.g., Gibbs and Bowers 2019; Baerg et al. 2020); how this relates to tornadogenesis is discussed below.

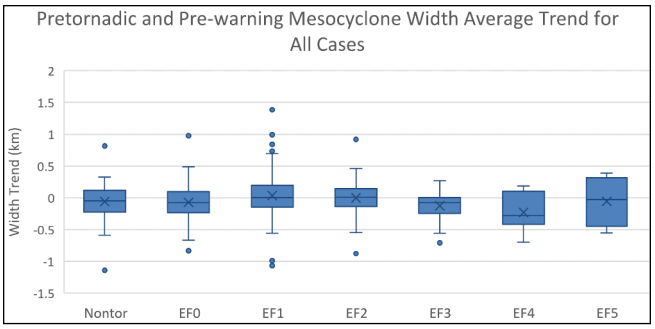

Figure 3. As in Fig. 2a, except for the average changes (km) in mesocyclone width during the pretornadic or pre-warning sampling time.

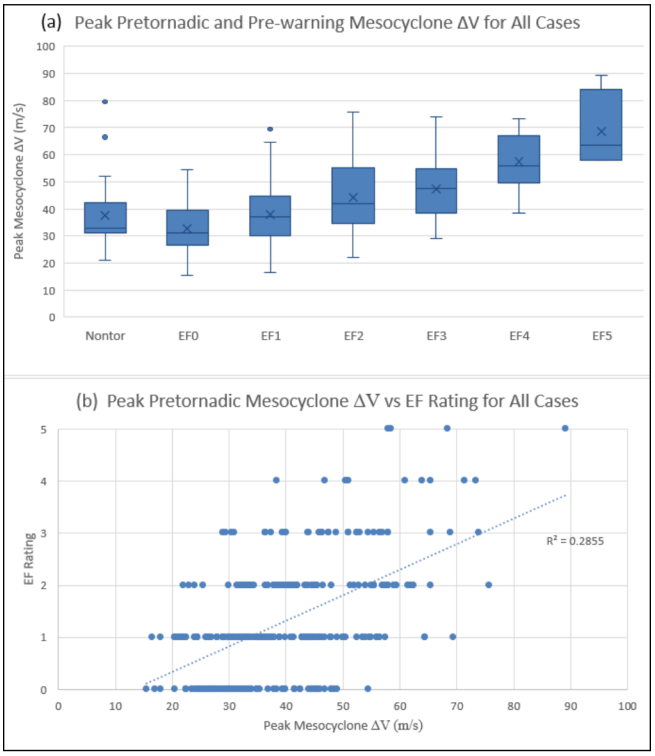

Figure 4. As in Fig. 2, except for the peak pretornadic or pre-warning mesocyclone intensity (differential velocity; m s^{-1}).

A relationship between pretornadic mesocyclone intensity (peak pretornadic ΔV; see Table 1) and the EF of the resultant tornado also is apparent in the box-and-whisker plot presented as Fig. 4a (also see Tables 3 and 4). However, as quantified by linear regression, the relationship is relatively weak (R^2 = 0.29; Fig. 4b); the relationship also is relatively weak (R^2 = 0.27) if average pretornadic ΔV is used in the linear regression. As a function of convective mode, the correlations are again higher for DSC (R^2 = 0.43), and lower for QLCS cases (R^2 = 0.09). As noted by ST20, pretornadic ΔV

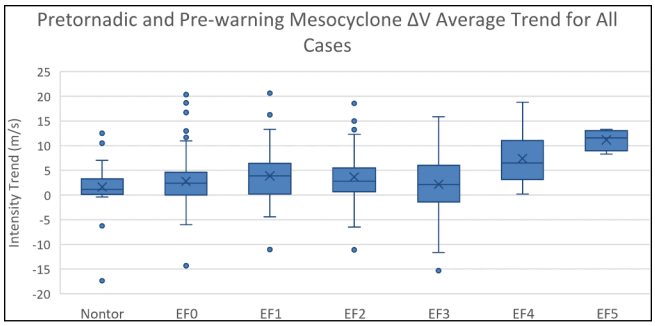

Figure 5. As in Fig. 2a, except for the average changes (m s^{-1}) in mesocyclone intensity during the pretornadic or pre-warning sampling time.

tends not to be as temporally consistent as width. On average, mesocyclone intensity tends to increase during the pretornadic sampling time (Fig. 5), which also has been demonstrated by Gibbs (2016) and Gibbs and Bowers (2019), which conforms to the expectation of tornadogenesis. Embedded within this trend, however, are fluctuations that may complicate real-time interpretation.

Because the foregoing analysis is fundamentally motivated by the principle of conservation of angular momentum or, equivalently, of circulation defined as:

$$V_T r_T = \Gamma = V_M r_M \quad (1)$$

where r_T and V_T (r_M and V_M) are, respectively, the radius and tangential windspeed of the tornado (pretornadic mesocyclone), and Γ is circulation (see Trapp et al. 2017), it would seem logical to also evaluate circulation itself. Figure 6a shows a box-and-whisker plot of average pretornadic mesocyclone circulation, which is represented here as the product between average differential velocity and average width, as a function of the EF of the resultant tornado. The plot indicates clear distinctions between pretornadic circulations for lower-end versus higher-end tornadoes, and consistently, the linear relationship between pretornadic mesocyclone circulation and EF is strong (R^2 = 0.62; Fig. 6b). Interestingly, the linear relationship between pretornadic mesocyclone width and intensity is relatively weak (R^2 = 0.29; not shown), indicating that wide pretornadic mesocyclones are not necessarily intense, and vice versa. These collective results seem to support the argument of Trapp et al. (2017) that a large-r_M, small-V_M product is more likely to explain a large value of mesocyclonic Γ than does a small-r_M, large-V_M product.

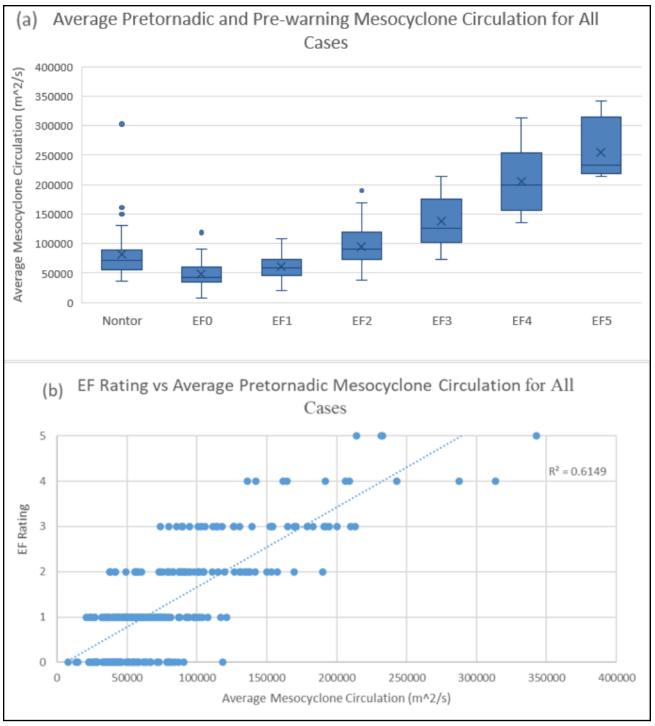

Figure 6. As in Fig. 2, except for the average pretornadic or pre-warning mesocyclone circulation (m^2 s^{-1}).

It is relevant to ask whether the circulation-conservation principle embodied in Eq. (1) also provides information about the tornado damage track. The box-and-whisker plots in Fig. 7 reveal a relationship between pretornadic mesocyclone width and tornado path width, such that the widest mesocyclones are associated with the widest damage paths. A relationship between pretornadic mesocyclone intensity and tornado path width also is suggested. Although not robust, the linear relationships between pretornadic mesocyclone characteristics and tornado path width (R^2 = 0.36 for mesocyclone width, R^2 = 0.21 for mesocyclone intensity) are at least relatively stronger than those between the pretornadic mesocyclone characteristics and tornado path length (R^2 = 0.25 for mesocyclone width, R^2 = 0.14 for mesocyclone intensity). This is perhaps not surprising given that for the cases in this dataset, the linear correlations between EF and tornado path width (R^2 = 0.43) are higher than those between EF and path length (R^2 = 0.28).

When viewing the average, pre-warning, mesocyclone width for nontornadic cases (Fig. 2a), there is clearly no distinction between nontornadic and tornadic storms, but there is separation from EF3+

Table 4. As in Table 3, except now separated by weak (EF0–1), strong (EF2–3), and violent (EF4–5) tornado intensity.

Parameter	EF0 to EF1 (194 cases)	EF2 to EF3 (92 cases)	EF4 to EF5 (14 cases)
Pretornadic Mesocyclone Width (km)	2.04, 0.37	3.01, 0.73	5.01, 0.59
Pretornadic Mesocyclone ΔV (m s^{-1})	35.8, 10.2	45.4, 11.5	60.5, 12.9
100-mb Mixed-Layer Convective Available Potential Energy (MLCAPE, J kg^{-1})	985, 249	1133, 250	1948, 404
100-mb Mixed-Layer Convective Inhibition (MLCIN, J kg^{-1})	–49, 23	–53, 25	–60, 32
Surface-based Convective Available Potential Energy (SBCAPE, J kg^{-1})	1317, 416	1330, 381	2507, 457
Surface-based Convective Inhibition (SBCIN, J kg^{-1})	–63, 34	–61, 30	–52, 23
Most-Unstable Convective Available Potential Energy (MUCAPE, J kg^{-1})	1538, 356	1593, 342	2771, 392
Most-Unstable Convective Inhibition (MUCIN, J kg^{-1})	–20, 16	–21, 17	–33, 13
0–3-km Convective Available Potential Energy (CAPE03, J kg^{-1})	54, 24	52, 21	49, 25
Lifted Index (LI, °C)	–2.69, 0.91	–2.42, 0.9	–3.85, 1.08
0–8-km Bulk Shear (S08, m s^{-1})	25, 2	28, 2.2	32, 2.1
0–6-km Bulk Shear (S06, m s^{-1})	23, 1.8	27, 2.1	29, 2.0
0–3-km Bulk Shear (S03, m s^{-1})	18, 1.9	21, 1.3	24, 2.1
0–1-km Bulk Shear (S01, m s^{-1})	13, 1.6	17, 1.2	16, 1.7
0–500-m bulk shear (S500, m s^{-1})	10, 1.4	12, 1.1	11, 1.3
Effective bulk shear (EBS, m s^{-1})	21, 2.3	25, 2.3	29, 2.1
Bunkers Right Storm Motion (BR, m s^{-1})	15, 1.3	17, 1.4	19, 1.1
0–6-km Mean Flow (06Mean, m s^{-1})	18, 1.1	21, 1.3	23, 0.9
0–1-km Storm Relative Helicity (01SRH, m^2 s^{-2})	204, 37	276, 43	254, 48
0–3-km Storm Relative Helicity (03SRH, m^2 s^{-2})	279, 48	372, 57	370, 67
0–500-m Storm Relative Helicity (0500SRH, m^2 s^{-2})	184, 38	191, 29	194, 40
Effective Storm Relative Helicity (ESRH, m^2 s^{-2})	196, 54	288, 67	307, 69
Effective Layer Top Height (ELT, m)	1528, 478	1677, 504	1991, 563
Effective Layer Depth (ELD, m)	1510, 414	1668, 453	2013, 526
0–2-km Storm Relative Wind (02SRW, m s^{-1})	10, 0.63	11, 0.73	11, 0.74
4–6-km Storm Relative Wind (46SRW, m s^{-1})	10, 0.82	10, 0.88	11, 0.83
9–11-km Storm Relative Wind (911SRW, m s^{-1})	16.3, 2.0	17, 2.3	17, 2.1
0–3-km Lapse Rate (03LR, °C km^{-1})	5.72, 0.38	5.70, 0.34	6.6, 0.4
3–6-km Lapse Rate (36LR, °C km^{-1})	6.21, 0.21	6.49, 0.24	7, 0.18
Lifting Condensation Level Height (LCLh, m)	389, 126	393, 120	706, 222
Level of Free Convection Height (LFCh, m)	1707, 760	1962, 829	1616, 504
Lifting Condensation Level to Level of Free Convection Height Difference (LCL-LFC, m)	1401, 815	1652, 811	946, 452
0–3-km Relative Humidity (03RH, %)	80, 4.5	80, 4.9	72, 4.9
3–6-km Relative Humidity (36RH, %)	65, 8.4	61, 8.7	42, 6.7
Lifting Condensation Level to Level of Free Convection Relative Humidity (LCL-LFC-RH, %)	83, 5.4	83, 6.2	78, 8.0
0–1-km Energy Helicity Index (01EHI)	1.01, 0.34	1.69, 0.45	2.73, 0.67
0–3-km Energy Helicity Index (03EHI)	1.51, 0.46	2.38, 0.58	4.14, 1.0
Fixed-layer Supercell Composite Parameter (SCPf)	2.07, 0.51	3.73, 0.87	7.14, 1.62
Effective-layer Supercell Composite Parameter (SCPe)	4.96, 1.77	8.29, 2.45	15, 3.4
Fixed-layer Significant Tornado Parameter (STPf)	1.27, 0.51	2.21, 0.81	4.1, 1.2
Violent Tornado Parameter (VTP)	0.89, 0.42	1.67, 0.66	4.23, 0.89
0–1-km Tornadic Energy Helicity Index (torEHI)	0.62, 0.29	1.43, 0.57	3.26, 1.0
Tornadic Tilting and Stretching Parameter (TTS)	1.65, 0.77	2.91, 1.1	2.82, 1.4
Critical Angle (CA, degrees)	67, 11	63, 8.4	62, 8.9

tornadoes. When viewing the peak, pre-warning, mesocyclone intensity (Fig. 4a), the distribution of intensities is similar to EF0–1 tornado-producing storms, but there is separation from EF2+ tornadoes. The pre-warning circulation (Fig. 6a), has a similar distribution to EF2 tornado-producing storms, similar to the pre-warning mesocyclone width, but still shows separation from EF3+ tornadoes. When considering the trend of pre-warning mesocyclone width (Fig. 3), there tended to still be a narrowing trend immediately prior to T-0 but to a lesser magnitude than tornadic cases and with more variability throughout the pre-warning time. There is still an increasing trend in the pre-warning mesocyclone intensity but to a lesser degree than during the pretornadic period of tornadic storms (Fig. 5). Importantly, the presence of these trends in nontornadic

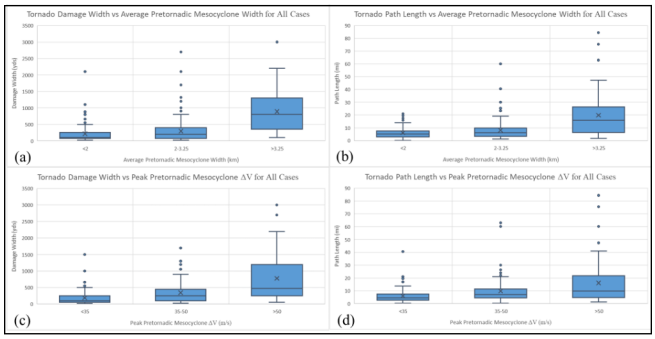

Figure 7. As in Fig. 2a, except for pretornadic: (a) mesocyclone width and tornado path width, (b) mesocyclone width and tornado path length, (c) mesocyclone intensity and tornado path width, and (d) mesocyclone intensity and tornado path length.

storms is consistent with radar signatures that would lead an operational forecaster to issue a tornado warning. The presence of narrowing and intensification is, therefore, not a trend specific to tornado-producing storms, but EF3+ tornadoes still had greater narrowing and intensification trends prior to tornadogenesis than the nontornadic storms prior to tornadogenesis failure. While mesocyclone width and intensity and their trends do not discriminate between nontornadic and tornadic storms, there still is separation of these variables between EF3+ tornado-producing storms and nontornadic and EF0–2 tornado-producing storms. Therefore, a weak, narrow mesocyclone would have a greater likelihood of being nontornadic or weakly tornadic than producing an EF3+ tornado, and a wide strong mesocyclone would have a greater likelihood of producing an EF3+ tornado than a weak tornado or no tornado at all.

An open question at this point is whether the pretornadic mesocyclone radar analyses are sensitive to the radar range and the associated changes in beam width and beam height, both of which impact how the vortex is sampled. To answer this, a similar radar range and beam height analysis to that of ST20 was completed in which the full dataset was divided into three range groups at the time of tornadogenesis as follows: 0–34 km (20% of cases), 35–69 km (48% of cases), and 70–100 km (32% of cases). Importantly, *there is no consistent reduction in the linear relationship between EF rating and the pretornadic mesocyclone width across the three range groups* (R^2 = 0.69, R^2 = 0.6, R^2 = 0.75, respectively; Fig. 8). The same can be said for the peak pretornadic mesocyclone ΔV, and in fact there is an increase in the coefficients of

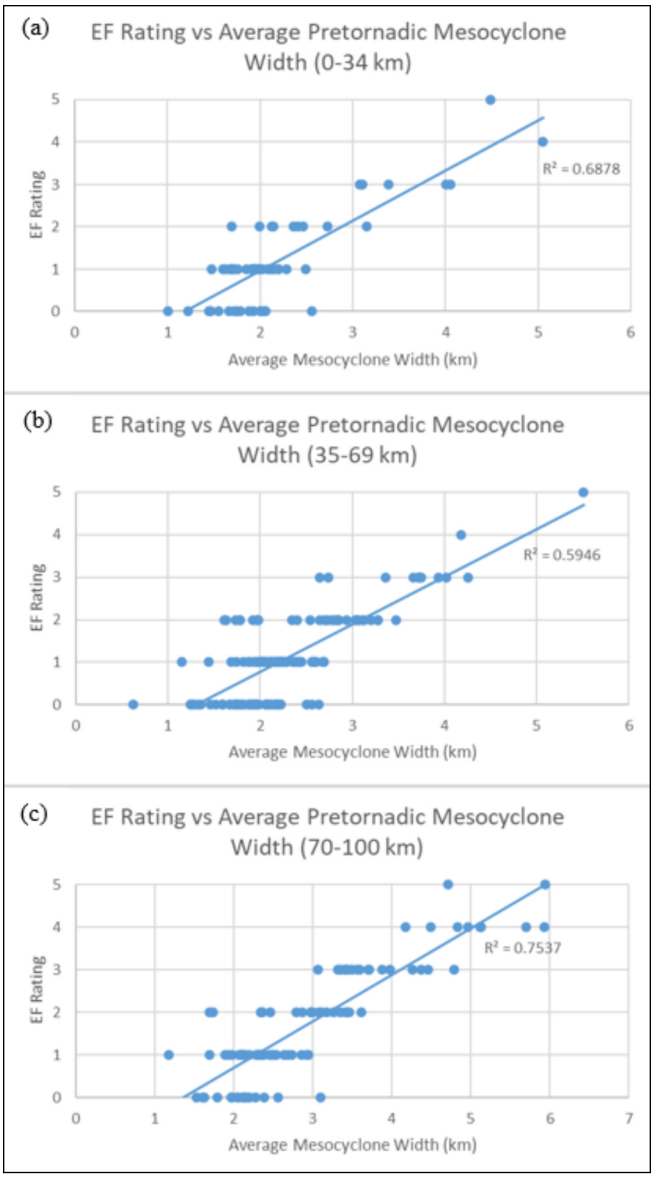

Figure 8. Scatterplot showing the linear relationship between the average pretornadic mesocyclone width (km) and the EF rating of the resultant tornado for all cases with a radar range of (a) 0–34 km, (b) 35–69 km, and (c) 70–100 km.

determination with radar range (R^2 = 0.21, R^2 = 0.25, R^2 = 0.31, respectively; not shown). Additionally, the linear regression between the pretornadic mesocyclone width and the radar range (not shown), has a weak positive linear relationship (R^2 = 0.13), which is reflected in the slight increase in the average pretornadic mesocyclone width of each EF category from the closest range group to the farthest range group (Table 5). There is no linear relationship between the peak pretornadic mesocyclone ΔV and the radar range

Table 5. The mean pretornadic mesocyclone width (km) of each range group separated by EF rating.

	EF0	EF1	EF2	EF3	EF4–5
0–34 km	1.76	1.92	2.34	3.53	4.77
35–70 km	1.85	2.16	2.58	3.6	4.85
70–100 km	2.1	2.3	2.87	3.75	5.1

(not shown). To directly consider whether cases of the same EF rating category have a similar distribution of distances from the radar, notice that the mean case distance is as follows: EF0-55 km, EF1-54 km, EF2-59 km, EF3-66 km EF4&5-69 km. While EF3–5 cases have larger mean distances, each EF category contains cases from each range group, implying that cases of all EF ratings experience the potential impacts and biases of the dependence of beam height and width with radar range, Therefore, the impact/bias of radar range on our overall conclusions should be limited.

A similar analysis can be completed for the height of the 0.5° beam at the approximate time and location of tornadogenesis, by dividing the dataset into the three 0.5° beam height groups of 0–500 m (34% of cases), 501–1000 m (43% of cases), and 1000+ m (23% of cases). As in the preceding analysis, there is no consistent decrease in the linear relationship between EF rating and the pretornadic mesocyclone width across the beam height groups ($R^2 = 0.71$, $R^2 = 0.59$, $R^2 = 0.76$, respectively; not shown). This also is true for the peak pretornadic mesocyclone ΔV ($R^2 = 0.18$, R2 = 0.28, $R^2 = 0.36$, respectively).

This exercise demonstrates more explicitly that the proposed relationship to EF rating is not limited to mesocyclones necessarily characterized as "near surface" or "low level" from the radar perspective. To this point it should be remembered that Doppler weather radar does not simply sample the atmosphere at discrete levels. A radar beam that is centered at 1000 m, for example, at some range is sampling target motion above and below that height. Thus, the framework suggested by this study to anticipate tornado intensity conditional on tornadogenesis can be applied to any storm within 100 km of a radar and the associated heights and depth of rotation that are viewed in that range. An important note here is the lack of non-significant tornadoes in the highest 0.5° beam height group. Only 10% of EF0s and 19% of EF1s (i.e., 15% of non-significant cases) were in the highest 0.5° beam height group demonstrating the difficulty in resolving the weaker, shallower mesocyclones of non-significant tornadoes when the lowest beam height is >1 km AGL.

It also is worthwhile to consider the impact of radar range and beam height on the separation of the mean pretornadic mesocyclone width and peak pretornadic mesocyclone ΔV with increasing EF rating. When viewing the change in the mean pretornadic mesocyclone width and the peak pretornadic mesocyclone ΔV with increasing EF rating for each range group, there is no pattern of change with range (Table 6). There is a similar result when considering the changes across the beam height groups. This demonstrates that the critical thresholds of width and intensity are not dependent on radar range and beam height.

Recalling the restriction imposed in section 2a that each tornado had to be the first produced by its respective parent storm, here we explore whether the relationships between pretornadic mesocyclone characteristics and EF rating apply when this restriction is removed. To do so, eight new cases from 2021 and 2022 in which more than one tornado was produced by the same storm were analyzed (Table 7). These cases were separated into two different scenarios based on the time between the dissipation of one tornado and the start of the following tornado. The first scenario encompasses storms wherein the dissipation of one tornado and the start of another tornado occurs over a period confined to less than two full volume scans (approximately 10 min). For cases in this scenario, the pretornadic mesocyclone characteristics prior to the first tornado would be applied to the maximum intensity of all tornadoes that were produced in quick succession. For example, from case #6 in Table 8, the first tornado (EF1) began at 2012 UTC and dissipated at 2026 UTC. The next tornado (EF3) began at 2033 UTC, so the time between the two tornadoes only included one full volume scan placing the case into the first scenario. The pretornadic characteristics prior to the first tornado were then associated with the maximum EF rating the storm produced, which in this instance was EF3. There are likely real-time situations where the determination that a tornado has dissipated and a new pretornadic period has begun could be done sooner than in two volume scans (especially when extra low-level scans are available via supplemental adaptive

Table 6. Change in the mean pretornadic mesocyclone width (km) and peak pretornadic mesocyclone intensity (ΔV, m s^{-1}) with increasing EF rating for each range group.

	EF1 - EF0	EF2 - EF1	EF3 - EF2	EF4&5 - EF3	Significant - Non-Significant
0–34 km	0.16 km, 1.3 m s^{-1}	0.42 km, 8.2 m s^{-1}	1.19 km, 1.1 m s^{-1}	1.24 km, 8.5 m s^{-1}	1.70 km, 12.4 m s^{-1}
35–70 km	0.3 km, 6.4 m s^{-1}	0.42 km, 7.0 m s^{-1}	1.02 km, 5.1 m s^{-1}	1.25 km, –1.0 m s^{-1}	1.67 km, 13.1 m s^{-1}
70–100 km	0.2 km, 4.7 m s^{-1}	0.57 km, 4.0 m s^{-1}	0.88 km, 3.1 m s^{-1}	1.35 km, 17.7 m s^{-1}	1.70 km, 14.3 m s^{-1}

Table 7. Case information for the eight tornadoes associated with storms that produced multiple tornadoes with tornadoes produced by the same storm having the same case number.

Case #	Date	State	County	Mode	Genesis Location (LAT, LON)	Dissipation Location (LAT, LON)	Path Length (miles)	Path Width (yds)
1	3/13/2021	Texas	Swisher	DSC	34.70, –101.99	34.95, –101.76	21.65	1500
1	3/13/2021	Texas	Randall	DSC	34.98, –101.73	35.04, –101.60	8.39	800
1	3/13/2021	Texas	Randall	DSC	35.01, –101.64	35.17, –101.53	13.17	1000
2	3/25/2021	Alabama	Hale	DSC	32.94, –87.58	33.01, –87.40	11.15	1400
2	3/25/2021	Alabama	Bibb	DSC	33.12, –87.17	33.50, –86.44	50.36	1100
2	3/25/2021	Alabama	Calhoun	DSC	33.7, –86.11	33.99, –85.54	38.44	1700
3	3/26/2021	Mississippi	Chilton	DSC	35.52, –90.25	32.89, –86.33	14.73	800
3	3/26/2021	Mississippi	Tallapoosa	DSC	33.09, –85.77	33.23, –85.26	31.13	1000
3	3/26/2021	Georgia	Heard	DSC	33.25, –85.19	33.45, –84.56	38.89	1850
4	3/27/2021	Arkansas	Mississippi	DSC	35.52, –90.25	35.52, –90.23	1.2	50
4	3/27/2021	Arkansas	Mississippi	DSC	35.54, –90.17	35.54, –90.15	1.1	80
4	3/27/2021	Arkansas	Mississippi	DSC	35.60, –90.08	35.60, –90.08	3.91	100
4	3/27/2021	Arkansas	Mississippi	DSC	35.66, –89.95	35.70, –89.87	4.93	125
5	12/11/2021	Arkansas	Jonesboro	DSC	35.47, –91.23	35.53, –91.13	6.69	150
5	12/11/2021	Arkansas	Poinsett	DSC	35.61, –90.93	35.62, –90.88	2.98	50
5	12/11/2021	Arkansas	Craighead	DSC	35.71, –90.73	35.75, –90.64	6.17	150
5	12/11/2021	Arkansas	Craighead	DSC	35.79, –90.55	36.40, –89.31	81.24	1800
5	12/11/2021	Tennessee	Obion	DSC	36.48, –89.14	37.61, –86.51	165.6	1760
6	3/21/2022	Texas	Palo Pinto	MUL	32.87, –98.53	32.96, –98.40	9.72	400
6	3/21/2022	Texas	Jack	MUL	33.04, –98.33	33.44, –97.97	34.51	880
7	3/21/2022	Texas	Travis	DSC	30.25, –97.48	30.36, –97.32	12.21	500
7	3/21/2022	Texas	Travis	DSC	30.37, –97.29	30.40, –97.21	5.57	50
8	3/31/2022	Alabama	Perry	DSC	32.55, –87.29	32.62, –87.23	6	500
8	3/31/2022	Alabama	Perry	DSC	32.75, –87.12	33.11, –86.86	29.36	1200

intra-volume low-level scans). It was found that this could possibly be done in a few of these cases allowing for new pretornadic characteristics to be applied to the subsequent tornado in the immediate next full volume scan after tornado dissipation, but in our demonstration if only one full volume scan is present between the end of one tornado and the start of another, this storm would fall under scenario 1. This was determined from keeping in mind that in a real-time scenario a forecaster would need to be able to say that a tornado has dissipated with some confidence so that the characteristics of the rotation are no longer being influenced by a tornado and are part of a new pretornadic period. This would realistically require a full volume scan (about 5–10 min) with potentially less time when extra low-level scans are available.

For cases in which at least two full volume scans are present between the dissipation of one tornado and the start of another, new pretornadic mesocyclone characteristics are applied to the subsequent tornado, and this defines scenario two. This scenario includes cases where 15 min pass between one tornado and the next, or even when ≥1 h has passed. The same methods are applied where up to four volume scans prior to tornadogenesis are analyzed. For example, from case #2 in Table 8, the same storm produced three EF3 tornadoes with more than two full volume scans between each tornado. Therefore, this storm fell into scenario two, and each of the three EF3 tornadoes produced by the same storm had their own unique pretornadic mesocyclone characteristics. Additionally, as demonstrated in case #3, one storm can encompass both scenarios over its lifetime.

As shown in Table 8, the pretornadic mesocyclone characteristics demonstrated in these examples of storms that produce multiple tornadoes are consistent with the relationships shown from the full dataset. The pretornadic widths and intensities fall within the

Table 8. Characteristics of the tornadoes and their pretornadic period for the eight tornadoes from storms that produced multiple tornadoes. Tornadoes produced by the same storm have the same case number, and subsequent tornadoes are labeled as scenario 1 or scenario 2 as described in section 3a.

Case #	Scenario	Genesis Time (UTC)	Dissipation Time (UTC)	EF Rating	Peak Est. Wind Speeds ($m\ s^{-1}$)	Start Time of Pretornadic Analysis	Average Pretornadic Mesocyclone Width (km)	Peak Pretornadic Mesocyclone ΔV ($m\ s^{-1}$)	Average Pretornadic Circulation ($m^2\ s^{-1}$)	# of Pretornadic Volume Scans
1	1st Tor.	21:15	22:00	2	51	20:55	3.41	55	137 301	4
1	1	22:00	22:14	1	49	20:55	3.41	55	137 301	4
1	1	22:06	22:34	0	36	20:55	3.41	55	137 301	4
2	1st Tor.	17:16	17:29	3	63	16:53	4.41	49.5	193 700	4
2	2	17:53	19:02	3	63	17:34	3.77	39.5	120 060	3
2	2	19:31	20:27	3	63	19:16	4.59	73.5	273 058	3
3	1st Tor.	2:01	2:21	2	51	1:39	3.02	48.5	125 796	4
3	2	2:55	3:33	2	56	2:44	5.23	59.5	272 981	2
3	1	3:37	4:30	4	76	2:44	5.23	59.5	272 981	2
4	1st Tor.	23:01	23:05	0	32	22:43	2.08	35.5	54 361	3
4	1	23:11	23:15	0	32	22:43	2.08	35.5	54 361	3
4	1	23:21	23:28	1	43	22:43	2.08	35.5	54 361	3
4	1	23:37	23:46	1	43	22:43	2.08	35.5	54 361	3
5	1st Tor.	0:17	0:25	UNK	UNK	23:49	4.75	46.5	195 597	4
5	1	0:36	0:43	0	29	23:49	4.75	46.5	195 597	4
5	1	0:57	1:04	1	45	23:49	4.75	46.5	195 597	4
5	1	1:07	2:36	4	76	23:49	4.75	46.5	195 597	4
5	1	2:41	5:47	4	85	0:49	4.75	46.5	195 597	4
6	1st Tor.	20:12	20:26	1	43	20:01	2.91	32.5	88 522	2
6	1	20:33	21:20	3	63	20:01	2.91	32.5	88 522	2
7	1st Tor.	23:30	23:50	2	58	23:13	3.41	50	14 224	3
7	1	23:54	0:04	0	34	23:13	3.41	50	14 224	3
8	1st Tor.	2:33	2:41	2	51	2:08	3.94	49.5	173 482	4
8	2	2:53	3:24	3	65	2:49	4.22	50	192 771	1

distributions from the larger dataset. Narrower, weaker pretornadic mesocyclones still tended to precede weaker tornadoes, and wider, stronger pretornadic mesocyclones still tended to precede stronger tornadoes in both scenarios described. Also, when these new cases are included with the original 300 cases, the results from the linear regression analyses do not change (not shown). Thus, the results from these additional cases support the idea that the pretornadic mesocyclone characteristics of a storm provide useful information about tornado intensity, conditional on tornadogenesis, for storms that produce multiple tornadoes. When using 2.5 km as a critical threshold of pretornadic mesocyclone width to separate non-significant from significant tornadoes, the average mesocyclone width from each pretornadic period could have been used to correctly predict the peak EF rating category (significant versus non-significant) associated with it. This is true for the maximum tornado intensity of multiple tornadoes from the same storm that occur in quick succession (scenario 1) or tornadoes that occur with new pretornadic periods between each tornado with each tornado having its own associated pretornadic characteristics (scenario 2). The hope is that these example cases at the very least demonstrate how the pretornadic mesocyclone characteristics and the methods of collecting them can be applied to subsequent tornadoes with a similar skill to when they are applied to the first tornado produced by a storm (while acknowledging that this is demonstrated in a few cases).

The radar-based results show much promise for real-time prediction of tornado intensity, conditional on tornadogenesis, during pretornadic stages of ongoing storms. Next, we consider whether near-storm environmental information may add predictive value toward this prediction goal.

b. Environments of significant versus nonsignificant tornadoes

To start, the overall results from our environmental analyses are consistent with previous studies (e.g., Thompson et al. 2012; Hampshire et al. 2018). Relative to non-significant tornadoes (EF0–1), significant tornadoes (EF2+) tend to occur in environments characterized by larger values of CAPE, midlevel temperature lapse rates, low-level and deep-layer vertical wind shear, storm-relative helicity (SRH), and composite parameters such as the SCP, STP, and energy

helicity index (EHI) (Figs. 9–11; also see Table 3). Greater effective-layer depth also was associated with EF2+ tornadoes (Fig. 10). On the other hand, low-level instability parameters (e.g., 0–3-km CAPE, 0–3-km lapse rates) do not appear to discriminate well between non-significant and significant tornadoes (Fig. 11).

Given the objectives of impact-based warnings (NWS 2011; also see the discussion by Gibbs and Bowers 2019), our goal herein is the successful binary prediction of significant (EF2+) versus non-significant (EF0–1) tornado intensity (section 3c). However, motivated by the results of Hampshire et al. (2018)—as well as by the clear separation in the pretornadic mesocyclone widths of weak (EF0–1) versus violent (EF4–5) tornadoes (Fig. 2a)—it also is instructive to view the environmental parameters over the three intensity categories of EF0–1 (weak), EF2–3 (strong), and EF4–5 (violent) (Figs. 12–14; also see Table 4); we do this with the caveat that the number of violent tornadoes in our dataset is approximately an order of magnitude less than that of weak tornadoes. CAPE parameters, effective-layer depth, 3–6-km temperature lapse rates, and all composite parameters show an increase across each of the three categories but a noticeably larger increase from EF2–3 to EF4–5 tornadoes (Figs. 13–14). The 0–8-, 0–6-, and 0–3-km bulk shear parameters, as well as effective bulk shear, show an even increase across each intensity category (Fig. 12). Lifted index, 0–3-km lapse rates, 0–3-km RH, 3–6-km RH, and the distance between the lifting condensation level (LCL) and the level of free convection (LFC) all show separation between environments of EF2–3 and EF4–5 tornadoes (while noting the limited sample size of 14 violent cases) but not between EF0–1 and EF2–3 tornadoes, highlighting how these parameters are especially relevant for the recognition of violent tornado environments (Fig. 14; Table 4). Low-level shear and SRH parameters, including effective SRH, show separation between environments of EF0–1 and EF2–3 tornadoes but not between EF2–3 and EF4–5 tornadoes, indicating that low-level shear may be a good discriminator between weak and strong tornado environments but not of violent tornado environments (Fig. 12). The importance of low-level instability/buoyancy parameters over low-level shear parameters for the identification of violent tornado environments is consistent with the relationships shown in Hampshire et el. (2018). These results highlight the importance of considering–when appropriate and feasible–the relationships between

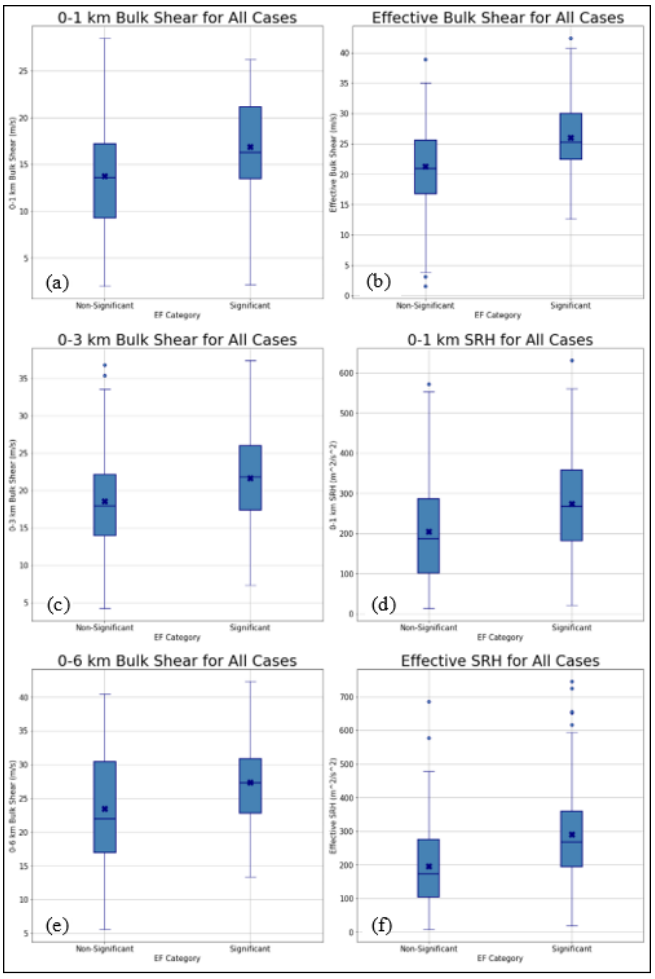

Figure 9. Box-and-whisker plot demonstrating the relationship, or lack thereof, between (a) S01 (m s^{-1}), (b) EBS (m s^{-1}), (c) S03 (m s^{-1}), (d) SRH01 (m^2 s^{-2}), (e) S06 (m s^{-1}), (f) ESRH (m^2 s^{-2}) and non-significant (EF0–1) and significant tornado intensity (EF2–5) for all cases. Refer to Table 2 for a description of these parameters, and how they were computed.

tornado intensity and the near-storm environment across three intensity categories instead of two.

For reference, the physical significance of the environmental parameters related to low-level vertical shear have been described, for example, by Markowski and Richardson (2014) and Markowski et al. (2002), although in the context of tornadogenesis rather than tornado intensification; the physical connection between low-level shear and rotating updraft width, and in turn between rotating updraft width and tornado intensification, has been demonstrated by Marion and Trapp (2019) and Trapp et al. (2017). Finally, predictors related to lapse rates and CAPE (i.e., individually and through the composite parameters, SCP, STP, and EHI)

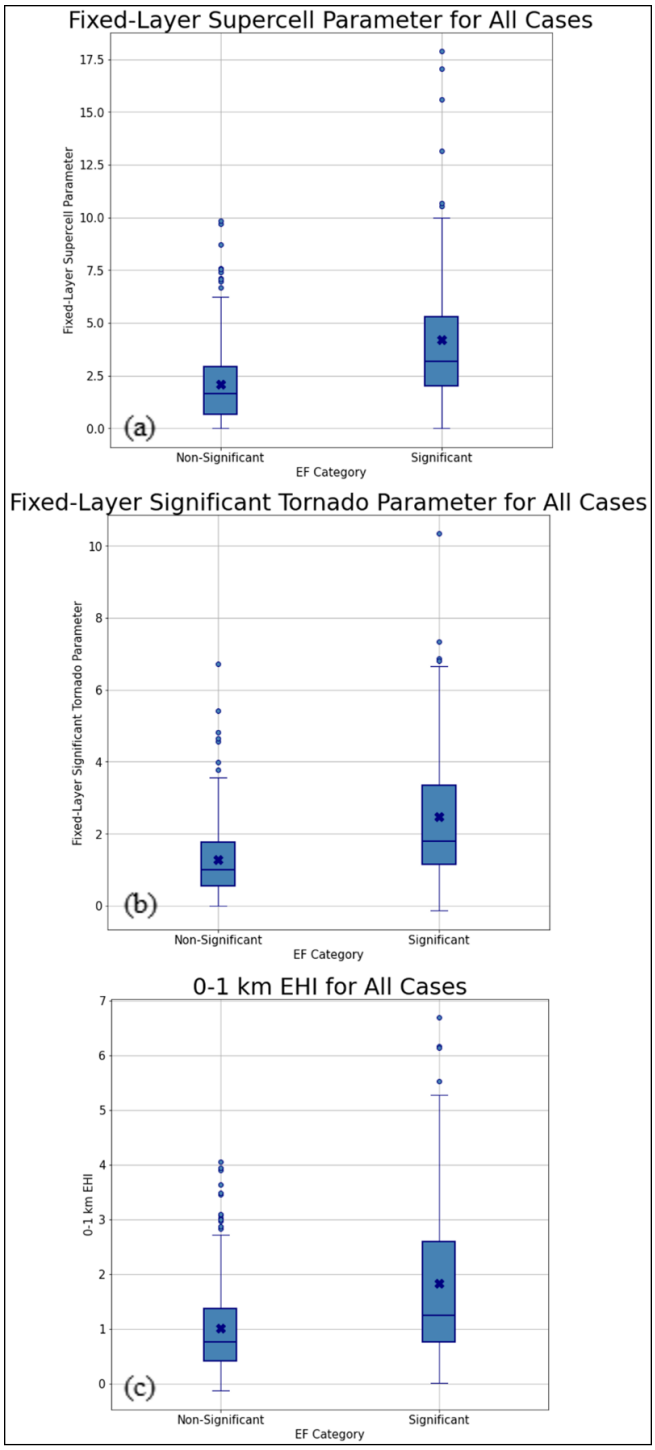

Figure 10. As in Fig. 9, except for (a) SCPf, (b) STPf, and (c) 01EHI.

are physically connected to tornado intensification through their contributions to vertical accelerations and, presumably, to vertical vortex stretching; CAPE also contributes to rotating updraft width (Marion and Trapp 2019).

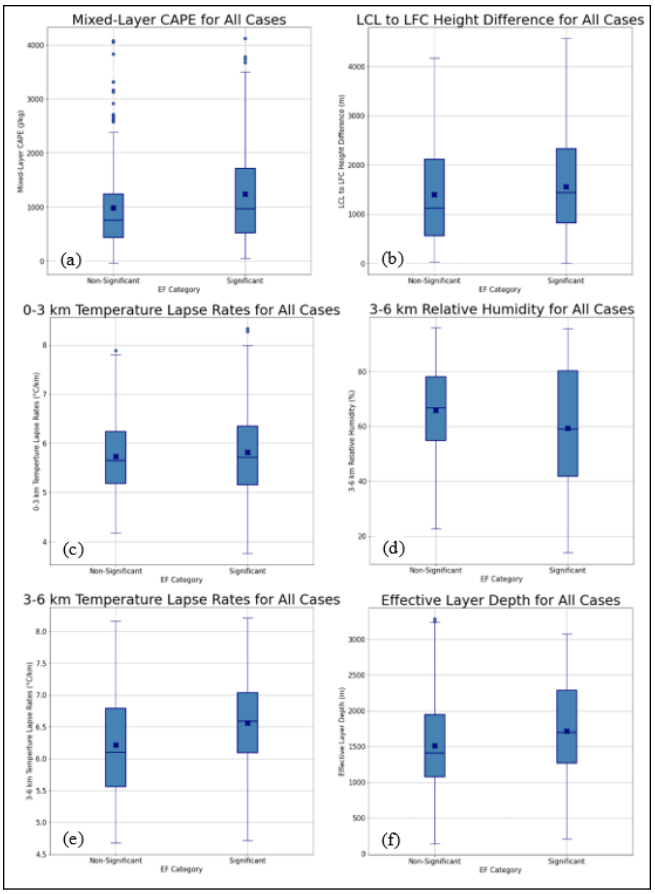

Figure 11. As in Fig. 9, except for (a) MLCAPE (J kg^{-1}), (b) LCL-LFC (m), (c) 03LR (°C km^{-1}), (d) 36RH (%), (e) 36LR (°C km^{-1}), (f) ELD (m).

Although LCL height may be more important for distinguishing between nontornadic and tornadic storms instead of non-significant and significant tornadoes (e.g., Thompson et al. 2003; Hampshire et al. 2018), it is still relevant to rectify the somewhat higher LCL heights for violent tornadoes (Table 4). The mean LCL heights for each of the three EF rating groups (weak, strong, violent) are all low LCL heights, even for the violent cases (706 m). While still low overall, the higher LCL heights for violent tornadoes in this dataset compared to weak and strong may be due to their occurrence outside of the summer months typically inhabited by richer moisture, the greater proportion of cases away from the very moist regimes of the Gulf States, and the occurrence of strong moisture gradients in several of the smaller sample of violent cases in this dataset (note the greater standard deviation for LCL height for the violent cases). Also, Davies (2006) found that significant tornadoes can occur in high LCL environments (>2 km) in the

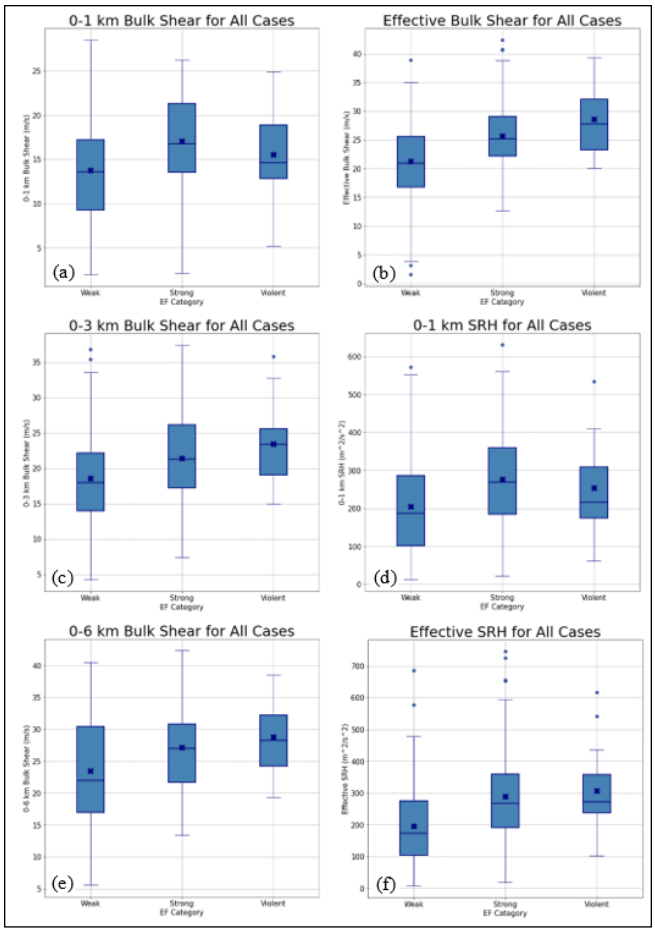

Figure 12. As in Fig. 9, except now categorized by weak (EF0–1), strong (EF2–3), and violent (EF4–5) tornado intensity.

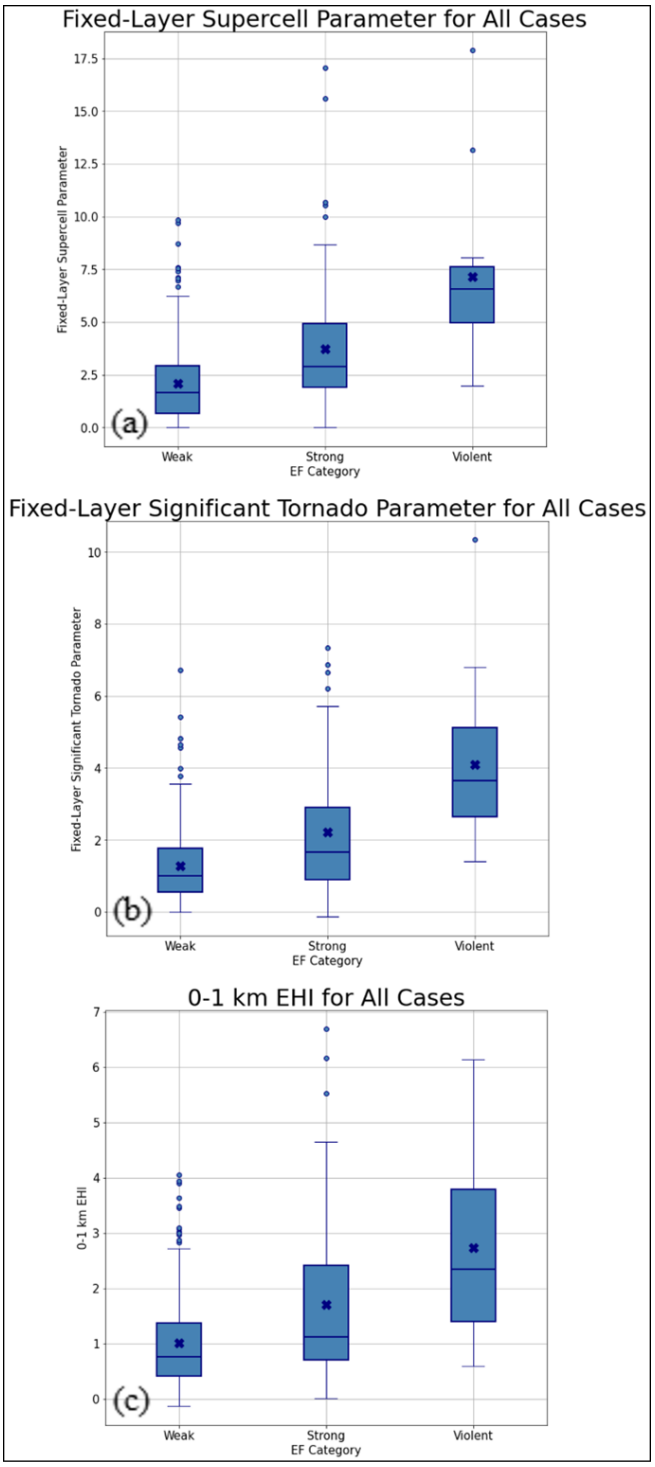

Figure 13. As in Fig. 10, except now categorized by weak (EF0–1), strong (EF2–3), and violent (EF4–5) tornado intensity.

presence of steep low-level lapse rates and adequate low-level moisture. Although no violent case (or any case at all), had a mean LCL height >2 km, three violent cases had mean LCL heights just over 1 km and these cases also had large low-level lapse rates and certainly adequate low-level moisture. Also, the distribution of LCL heights for the violent cases in this dataset are consistent with the results of Grams et al. (2012).

Upon further stratifying these results across the three convective modes of DSC, QLCS, and MUL, the same relationships between the three intensity categories generally apply (not shown). The only exception is that the 0–3- and 3–6-km lapse rates only show a noticeable increase from strong to violent tornadoes for DSC cases. An interesting relationship seen between convective mode and tornado intensity is that strong QLCS tornadoes are associated with greater low-level shear and SRH but lower CAPE than strong DSC tornadoes. There are no clear differences seen with composite parameters between the convective modes. This indicates that significant QLCS tornadoes tend to occur in high-shear–low-CAPE environments, as also shown by Thompson et al. (2012), Davis and

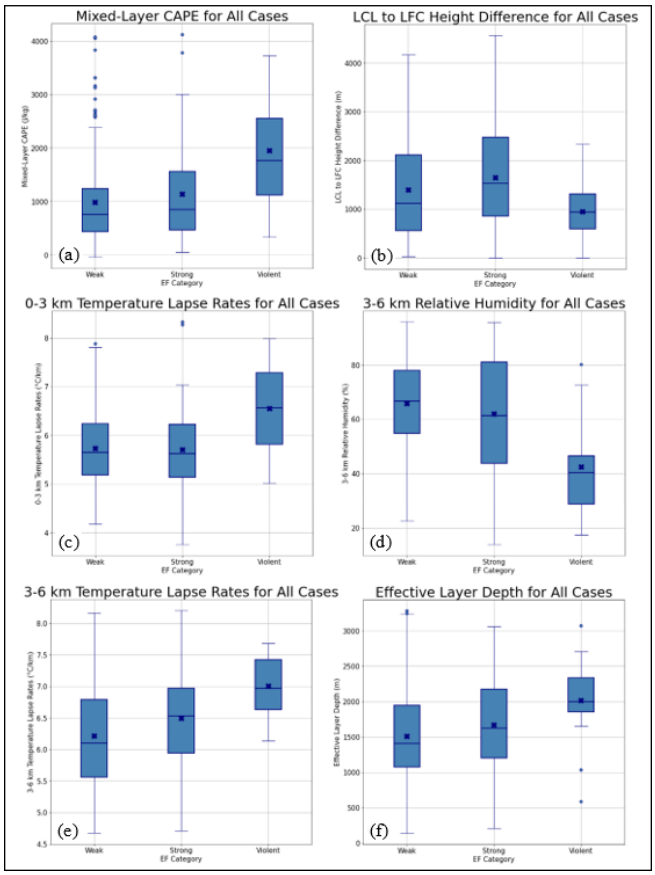

Figure 14. As in Fig. 11, except now categorized by weak (EF0–1), strong (EF2–3), and violent (EF4–5) tornado intensity.

Parker (2014), and Sherburn and Parker (2019). MUL cases did not include any violent tornadoes, but the same parameters that show separation between EF0–1 and EF2–3 tornadoes for all cases show similar relationships for MUL cases. Additionally, QLCS cases only include one violent tornado (associated with a deep, strong rotating updraft in the midlevels of the storm and rapid development of rotation across the lowest three elevation angles immediately preceding tornadogenesis).

4. Discussion

The operational implementation of these results for the purposes of tornado-intensity prediction is straightforward. Environmental parameters are easily obtainable from observed soundings or operational-model grids using software packages such as MetPy (May et al. 2022) and SHARPpy (Blumberg et al. 2017), and indeed are already routinely computed as part of the SPC mesoanalysis (Bothwell et al. 2002). In principle, the radar-based predictors also are relatively easily obtainable, but would need to be quantified in real time, using automated approaches. Mesocyclone width and intensity are attributes computed within the (original) mesocyclone detection algorithm (Stumpf et al. 1998), and presumably could be extracted and made available to forecasters. The time series of these attributes for identified and tracked mesocyclones are of particular relevance. We envision the need for a moving time average of the width (and intensity) of identified mesocyclones (calculated using up to the most recent four volume scans) and their temporal variability, which would then be the key metrics used to predict intensity upon tornadogenesis. For example, taken alone, a mesocyclone that is narrow (e.g., diameter <1.5 km) over its lifetime would not be expected to be associated with a significant tornado, and this conclusion still remains even with the added consideration of nontornadic cases. When applying these methods to a storm that produces multiple tornadoes, the metrics could be paused when a tornado is detected and resumed upon the dissipation of the tornado so that the characteristics of the mesocyclone are not influenced by the presence of a tornado. The environmental predictors are available hourly and thus could provide lead time of up to 1 h. The lead time provided by the radar predictors (which would update approximately every 5 min) may be from about 4 min up to the time when the mesocyclone is first present when a running mean of the mesocyclone characteristics could begin.

Most often, information about tornado intensity is communicated once the presence of a significant tornado is confirmed using the spotter network and tornadic debris signatures, but this is only once the tornado has been in progress. The information gained from the pretornadic analysis demonstrated in this study would allow an operational forecaster to be aware of and communicate this information about potential tornado intensity in warning text to the public before a tornado develops to better protect life and property.

Realization of the predicted intensity is conditional on tornadogenesis, so the recommended intensity prediction procedure should be coupled to a tornadogenesis prediction. There have been several recent machine learning applications specifically involving the prediction or likelihood of tornadogenesis (e.g., Lagerquist et al. 2018, 2020; Steinkruger et al. 2020; Coffer et al. 2021). The predictors range from radar-observed storm attributes to convection-allowing

model variables such as updraft helicity. Additionally, simple observational approaches for the prediction of tornadogenesis outside of machine learning include the use of radar signatures such as the ZDR arc and column and KDP foot (Crowe et al. 2012; Homeyer et al. 2020; Van Den Broeke 2020) and trends in mesocyclone characteristics such as width, depth, and intensity (Gibbs and Bowers 2019; Sandmæl et al. 2019). Also, the inclusion of an analysis of nontornadic cases in this study allows for an understanding of how the radar metrics used to anticipate tornado intensity relate to tornadogenesis and stresses the need for additional tools for anticipating tornadogenesis to be coupled with the tornado intensity anticipation tools outlined in this study. Additionally, it should be highlighted that after applying the prognostic techniques of this study to anticipate tornado intensity that diagnosing the tornado intensity of the later formed tornado is equally important to validate the forecasted intensity. As highlighted earlier, there are several previous studies that discuss diagnosing the intensity of ongoing tornadoes using radar characteristics such as velocity and correlation coefficient as well as the near storm environment and population density (e.g., Toth et al. 2013, Smith et al. 2020a,b).

5. Conclusions

Analyses of Doppler radar data and environmental parameters for 300 tornado cases were used to propose an alternative framework for tornado intensity prediction during pretornadic stages of ongoing storms. This framework is founded on the robust relationship between pretornadic mesocyclone width and tornado intensity, which is based on theoretical arguments posed by Trapp et al. (2017). Specifically, in the linear regression between (average) pretornadic mesocyclone width and the EF of the resultant tornado, the coefficient of determination (R^2) is 0.69. In contrast, the linear relationship between pretornadic mesocyclone intensity (peak pretornadic ΔV) and EF scale is much weaker, as quantified by an R^2 of 0.29.

The additional analysis of 35 nontornadic storms revealed that mesocyclone width and intensity could not be used to discriminate between nontornadic and tornadic storms, and their trends could not be used to anticipate tornadogenesis. On the other hand, this analysis revealed a distinct separation of the pre-warning mesocyclone widths and intensities of nontornadic storms from the pretornadic mesocyclone widths and intensities of EF3+ tornado-producing storms. This null case analysis increases the understanding and applicability of these methods for anticipating tornado intensity in ongoing thunderstorms. Future exploration of how the mesocyclone attributes explored in this study relate to tornadogenesis would certainly be beneficial through an expansion of the nontornadic dataset, which could further reveal any relationships between mesocyclone width and intensity and tornadogenesis as well as help identify critical thresholds of trends in mesocyclone width and intensity for the anticipation of tornadogenesis and tornado intensity.

Environmental information for each of the cases in this dataset also was used to explore relationships between environmental parameters and tornado intensity. As also noted by Hampshire et al. (2018), such relationships depend in part on how the tornado-intensity categories are distributed [i.e., significant (EF2+) versus nonsignificant (EF0–1), or weak (EF0–1) versus strong (EF2–3) versus violent (EF4–5)]. So, for example, low-level shear parameters (bulk shear, SRH) discriminate the environments of significant tornadoes from nonsignificant tornadoes, but not the environments of violent tornadoes from strong tornadoes. On the other hand, thermodynamic parameters such as CAPE (SB, ML, MU, 0–3), as well as the composite parameters that include CAPE, discriminate the environments of violent tornadoes from strong tornadoes.

It is important to mention some of the limitations of this study as well. First, the spatial constraints of being able to adequately resolve pretornadic characteristics in the lowest levels of a storm using WSR-88Ds limit the pretornadic characteristics used to generally only be from storms within about 100 km of a radar site. The pretornadic radar characteristics used in this study may not always be resolvable for every storm. Also, the limitations of the United States tornado report dataset are acknowledged, well-known, and discussed in recent decades (e.g., Doswell and Burgess 1988; Smith et al. 2012; Potvin et al. 2019). Tornado reports do not consistently capture tornado intensity because the EF scale is damage based (McDonald et al. 2010; Edwards et al. 2013; Wurman et al. 2021), and tornadoes of the same pathlength, width, and intensity can produce different damage depending upon their location (Strader and Ashley 2018; Strader et al. 2018). Additionally, the time and location of tornadogenesis may not always be accurate. It is important to keep

these limitations in mind when interpreting this study.

Operational implementation of this framework for the purposes of impact-based warnings will require real-time, automated quantification of mesocyclone width in addition to intensity and other attributes. This should be straightforward, given the construction of the mesocyclone detection algorithm. The information given from pretornadic characteristics of a storm and its surrounding environment can provide useful information about potential tornado intensity to an operational forecaster before a tornado develops that can be communicated and used in warning decisions and text to better protect life and property.

The datasets used in this study are being applied to tornado-intensity prediction through machine learning applications in a separate study (e.g., Sessa and Trapp 2022). Several machine learning algorithms are being implemented and used to examine their skill in predicting significant or non-significant tornado intensity for a given storm. Models such as logistic regression, random forests, and gradient-boosted decision trees are found to be the most skilled classifier as measured by several binary classification metrics and performance diagrams. Adequacy of model training, model reliability, and the significance of results also are being explored. Finally, feature importance and the decision-making process within each model is being analyzed to help reveal a more physical understanding of the model performance and results, as well as relationships between the predictors and tornado intensity including the establishment of critical thresholds of predictors. Results demonstrate that the pretornadic radar predictors of mesocyclone width and differential velocity are the most important followed by environmental vertical wind shear and composite parameters. This additional work utilizing the relationships outlined in this study and combining the datasets through the power of machine learning, thus far, demonstrates a skilled binary prediction of tornado intensity, conditioned upon tornadogensis, and the potential for these machine learning applications to become a helpful resource in an operational setting. Additional future work could involve the continued exploration of any potential relationships between pretornadic mesocyclone characteristics, specifically width and intensity, and tornadogenesis as well as further testing the relationships shown in this study on a larger sample of multiple tornado producing storms as well as other independent datasets. The development of a larger climatology of pretornadic mesocyclone characteristics would certainly be beneficial to the operational implementation of this work as well.

Acknowledgments. This work was supported in part by NOAA award NA17OAR4590195. The authors acknowledge the contribution of Mr. Jared Stickney and Mr. Anay Patel toward the manual analysis of the Doppler radar data. We also thank the three reviewers for their helpful comments and suggestions.

REFERENCES

Anderson-Frey, A. K., and H. Brooks, 2019: Tornado fatalities: An environmental perspective. *Wea. Forecasting*, **34**, 1999–2015, Crossref.

____, Y. P. Richardson, A. R. Dean, R. L. Thompson, and B. T. Smith, 2016: Investigation of near-storm environments for tornado events and warnings. *Wea. Forecasting*, **31**, 1771–1790, Crossref.

Ashley, W. S., 2007: Spatial and temporal analysis of tornado fatalities in the United States: 1880–2005. *Wea. Forecasting*, **22**, 1214–1228, Crossref.

Baerg, B. M., W. P. Gargan, A. E. Cohen, R. L. Thompson, B. T. Smith, A. E. Gerard, C. J. Schultz, L. A. Kelly, and H. V. Nepaul, 2020: Radar-based, storm-scale circulation and tornado-probability tendencies preceding tornadogenesis in Kansas and Nebraska. *Electronic J. Severe Storms Meteor*., **15** (3), 1–23, Crossref.

Benjamin, S. G., and Coauthors, 2004: An hourly assimilation–forecast cycle: The RUC. *Mon. Wea. Rev*., **132**, 495–518, Crossref.

____, and ____, 2016: A North American hourly assimilation and model forecast cycle: The Rapid Refresh.. *Mon. Wea. Rev*., **144**, 1669–1694, Crossref.

Blumberg, W. G., K. T. Halbert, T. A. Supinie, P. T. Marsh, R. L. Thompson, and J. A. Hart, 2017: SHARPpy: An open source sounding analysis toolkit for the atmospheric sciences. *Bull. Amer. Meteor. Soc*. **98**, 1625–1636, Crossref.

Bothwell, P. D., J. A. Hart, and R. L. Thompson, 2002: An integrated three-dimensional objective analysis scheme in use at the Storm Prediction Center. Preprints, *21st Conf. on Severe Local Storms*, San Antonio, TX, Amer. Meteor. Soc., J117–J120. [Available online at http://ams.confex.com/ams/pdfpapers/47482.pdf].

Brooks, H. E., C. A. Doswell III, and J. Cooper, 1994: On the environments of tornadic and nontornadic mesocyclones. *Wea. Forecasting*, **9**, 606–618, Crossref.

____, ___, and M. P. Kay, 2003: Climatological estimates of local daily tornado probability for the United States. *Wea. Forecasting*, **18**, 626–640, Crossref.

Brotzge, J. A., S. E. Nelson, R. L. Thompson, and B. T. Smith, 2013: Tornado probability of detection and lead time as a function of convective mode and environmental parameters. *Wea. Forecasting*, **28**, 1261–1276, Crossref.

Coffer, B., M. Kubacki, Y. Wen, T. Zhang, C. A. Barajas, and M. K. Gobbert, 2021: Machine learning with feature importance analysis for tornado prediction from environmental sounding data. *Proc. Appl. Math. Mech*., **20**, 1–2, Crossref.

Cohen, A. E., J. B. Cohen, R. L. Thompson, and B. T. Smith, 2018: Simulating tornado probability and tornado wind speed based on statistical models. *Wea. Forecasting*, **33**, 1099–1108, Crossref.

Coniglio, M. C., 2012: Verification of RUC 0–1-h forecasts and SPC mesoscale analyses using VORTEX2 soundings. *Wea. Forecasting*, **27**, 667–683, Crossref.

____, and M. D. Parker, 2020: Insights into supercells and their environments from three decades of targeted radiosonde observations. *Mon. Wea. Rev*., **148**, 4893–4915, Crossref.

Crowe, C. C., C. J. Schultz, M. Kumjian, L. D. Carey, and W. A. Petersen, 2012: Use of dual-polarization signatures in diagnosing tornadic potential. *Electronic J. Operational Meteor*., **13** (5), 57–78, [Available online at http://nwafiles.nwas.org/ej/pdf/2012-EJ5.pdf].

Davies, J. M., 2006: Tornadoes in environments with helicity and/or high LCL heights. *Wea. Forecasting*, **21**, 579–594, Crossref.

Davis, J. M., and M. D. Parker, 2014: Radar climatology of tornadic and nontornadic vortices in high-shear, low-CAPE environments in the mid-Atlantic and southeastern United States. *Wea. Forecasting*, **29**, 828–853, Crossref.

Doswell, C. A., III, and D. W. Burgess, 1988: On some issues of United States tornado climatology. *Mon. Wea. Rev*., **116**, 495–501, Crossref.

Edwards, R., J. G. LaDue, J. T. Ferree, K. Scharfenberg, C. Maier, and W. L. Coulbourne, 2013: Tornado intensity estimation: Past, present, and future. *Bull. Amer. Meteor. Soc*., **94**, 641–653, Crossref.

French, M. M., and D. M. Kingfield, 2021: Tornado formation and intensity prediction using polarimetric radar estimates of updraft area. *Wea. Forecasting*, **36**, 2211–2231, Crossref.

Gibbs, J. G., 2016: A skill assessment of techniques for real-time diagnosis and short-term prediction of tornado intensity using the WSR-88D. *J. Operational Meteor*., **4**, 170–181, Crossref.

____, and B. R. Bowers, 2019: Techniques and thresholds of significance for using WSR-88D velocity data to anticipate significant tornadoes. *J. Operational Meteor*., **7**, 117–137, Crossref.

Grams, J. S., R. L. Thompson, D. V. Snively, J. A. Prentice, G. M. Hodges, and L. J. Reames, 2012: A climatology and comparison of parameters for significant tornado events in the United States. *Wea. Forecasting*, **27**, 106–123, Crossref.

Hampshire, N. L., R. M. Mosier, T. M. Ryan, and D. E. Cavanaugh, 2018: Relationship of low-level instability and tornado damage rating based on observed soundings. *J. Operational Meteor*., **6**, 1–12, Crossref.

Homeyer, C. R., T. N. Sandmæl, C. K. Potvin, and A. M. Murphy, 2020: Distinguishing characteristics of tornadic and nontornadic supercell storms from composite mean analyses of radar observations. *Mon. Wea. Rev*., **148**, 5015–5040, Crossref.

King, A. T. and A. D. Kennedy, 2019: North American supercell environments in atmospheric reanalyses and RUC-2. *J. Appl. Meteor. Climatol*., **58**, 71–92, Crossref.

Kingfield, D. M., and J. G. LaDue, 2015: The relationship between automated low-level velocity calculations from the WSR-88D and maximum tornado intensity determined from damage surveys. *Wea. Forecasting*, **30**, 1125–1139, Crossref.

Laflin, J. M., 2013: Verification of RAP model soundings in preconvective environments. *J. Operational Meteor*., **1**, 66–70, Crossref.

Lagerquist, R. A., C. R. Homeyer, A. Mcgovern, C. K. Potvin, T. Sandmæl, and T. M. Smith. 2018: Deep learning for real-time storm-based tornado prediction. *29th Conf. on Severe Local Storms*, Stowe, VT, Amer. Meteor. Soc., 138. [Available online at https://ams.confex.com/ams/29SLS/meetingapp.cgi/Paper/348817].

____, A. McGovern, C. R. Homeyer, D. J. Gagne II, and T. Smith, 2020: Deep learning on three-dimensional multiscale data for next-hour tornado prediction. *Mon. Wea. Rev*., **148**, 2837–2861, Crossref.

Marion, G. R., and R. J. Trapp, 2019: The dynamical coupling of convective updrafts, downdrafts, and cold pools in simulated supercell thunderstorms. *J. Geophys. Res. Atmos*., **124**, 664–683, Crossref.

____, ____, and S. W. Nesbitt, 2019: Using overshooting top area to discriminate potential for large, intense tornadoes. *Geophys. Res. Lett*., **46**, 12 520–12 526, Crossref.

Markowski, P. M., and Y. P. Richardson, 2014: The influence of environmental low-level shear and cold pools on tornadogenesis: Insights from idealized simulations. *J. Atmos. Sci*., **71**, 243–275, Crossref.

____, J. M. Straka, and E. N. Rasmussen, 2002: Direct surface thermodynamic observations within the rear-flank downdrafts of nontornadic and tornadic supercells. *Mon. Wea. Rev.*, **130**, 1692–1721, Crossref.

____, C. Hannon, J. Frame, E. Lancaster, A. Pietrycha, R. Edwards, and R. L. Thompson, 2003: Characteristics of vertical wind profiles near supercells obtained from the Rapid Update Cycle. *Wea. Forecasting*, **18**, 1262–1272, Crossref.

May, R. M., and Coauthors, 2022: MetPy: A meteorological Python library for data analysis and visualization. *Bull. Amer. Meteor. Soc.*, **103**, E2273–E2284, Crossref.

McDonald, J. R., K. C. Mehta, D. A. Smith, and J. A. Womble, 2010: The enhanced Fujita scale: Development and implementation. Forensic Engineering 2009: Pathology of the Built Environment, S.-E. Chen et al., Eds., ASCE, 719–728, Crossref.

NWS, 2011: Joplin, Missouri, Tornado – May 22, 2011. NOAA/NWS Central Region Service Assessment, 41 pp. [Available online at www.weather.gov/media/publications/assessments/Joplin_tornado.pdf.]

Nowotarski, C. J., and A. A. Jensen, 2013: Classifying proximity soundings with self-organizing maps toward improving supercell and tornado forecasting. *Wea. Forecasting*, **28**, 783–801, Crossref.

Parker, M. D., 2014: Composite VORTEX2 supercell environments from near-storm soundings. *Mon. Wea. Rev.*, **142**, 508–529, Crossref.

Potvin, C. K., K. L. Elmore, and S. J. Weiss, 2010: Assessing the impacts of proximity sounding criteria on the climatology of significant tornado environments. *Wea. Forecasting*, **25**, 921–930, Crossref.

____, C. Broyles, P. S. Skinner, H. E. Brooks, and E. Rasmussen, 2019: A Bayesian hierarchical modeling framework for correcting reporting bias in the U.S. tornado database. *Wea. Forecasting*, **34**, 15–30, Crossref.

Reames, L. J., 2017: Diurnal variations in severe weather forecast parameters of Rapid Update Cycle-2 tornado proximity environments. *Wea. Forecasting*, **32**, 743–761, Crossref.

Sandmæl, T. N., C. R. Homeyer, K. M. Bedka, J. M. Apke, J. R. Mecikalski, and K. Khlopenkov, 2019: Evaluating the ability of remote sensing observations to identify significantly severe and potentially tornadic storms. *J. Appl. Meteor. Climatol.*, **58**, 2569–2590, Crossref.

Sessa, M. F., and R. J. Trapp, 2020: Observed relationship between tornado intensity and pretornadic mesocyclone characteristics. *Wea. Forecasting*, **35**, 1243–1261, Crossref.

____, and ____, 2022: The prediction of potential tornado intensity using machine learning. *21st Conf. on Artificial Intelligence for Environmental Science*, Houston, TX, Amer. Meteor. Soc., 122. [Available online at https://ams.confex.com/ams/102ANNUAL/meetingapp.cgi/Paper/396133].

Sherburn, K. D., and M. D. Parker, 2019: The development of severe vortices within simulated high-shear, low-CAPE convection. *Mon. Wea. Rev.*, **147**, 2189–2216, Crossref.

Simmons, K. M., and D. Sutter, 2011: Economic and Societal Impact of Tornadoes. *Amer. Meteor. Soc.*, 296 pp, Crossref.

Smith, B. T, R. L. Thompson, J. S. Grams, C. Broyles, and H. E. Brooks, 2012: Convective modes for significant severe thunderstorms in the contiguous United States. Part I: Storm classification and climatology. *Wea. Forecasting*, **27**, 1114–1135, Crossref.

____, ____, A. R. Dean, and P. T. Marsh, 2015: Diagnosing the conditional probability of tornado damage rating using environmental and radar attributes. *Wea. Forecasting*, **30**, 914–932, Crossref.

____, ____, D. A. Speheger, A. R. Dean, C. D. Karstens, and A. K. Anderson-Frey, 2020a: WSR-88D tornado intensity estimates. Part I: Real-time probabilities of peak tornado wind speeds. *Wea. Forecasting*, **35**, 2479–2492, Crossref.

____, ____, ____, ____, ____, and ____, 2020b: WSR-88D Tornado Intensity Estimates. Part II: Real-time applications to tornado warning time scales. *Wea. Forecasting*, **35**, 2493–2506, Crossref.

Steinkruger, D., P. Markowski, and G. Young, 2020: An artificially intelligent system for the automated issuance of tornado warnings in simulated convective storms. *Wea. Forecasting*, **35**, 1939–1965, Crossref.

Strader, S. M., and W. S. Ashley, 2018: Finescale assessment of mobile home tornado vulnerability in the central and southeast United States. *Wea. Climate Soc.*, **10**, 797–812, Crossref.

____, ____, T. J. Pingel, and A. J. Krmenec, 2018: How land use alters the tornado disaster landscape. *Appl. Geogr.*, **94**, 18–29, Crossref.

Stumpf, G. J., A. Witt, E. D. Mitchell, P. L. Spencer, J. T. Johnson, M. D. Eilts, K. W. Thomas, and D. W. Burgess, 1998: The National Severe Storms Laboratory Mesocyclone Detection Algorithm for the WSR-88D. *Wea. Forecasting*, **13**, 304–326, Crossref.

Thompson, R. L., R. Edwards, J. A. Hart, K. L. Elmore, and P. Markowski, 2003: Close proximity soundings within supercell environments obtained from the Rapid Update Cycle. *Wea. Forecasting*, **18**, 1243–1261, Crossref.

____, C. M. Mead, and R. Edwards, 2007: Effective storm-relative helicity and bulk shear in supercell thunderstorm environments. *Wea. Forecasting*, **22**, 102–115, Crossref.

____, B. T. Smith, J. S. Grams, A. R. Dean, and C. Broyles, 2012: Convective modes for significant severe thunderstorms in the contiguous United States. Part II: Supercell and QLCS tornado environments. *Wea. Forecasting*, **27**, 1136–1154, Crossref.

____, and Coauthors, 2017: Tornado damage rating probabilities derived from WSR-88D data. *Wea. Forecasting*, **32**, 1509–1528, Crossref.

Toth, M., R. J. Trapp, J. Wurman, and K. A. Kosiba, 2013: Comparison of mobile-radar measurements of tornado intensity with corresponding WSR-88D measurements. *Wea. Forecasting*, **28**, 418–426, Crossref.

Trapp, R. J., 1999: Observations of nontornadic low-level mesocyclones and attendant tornadogenesis failure during VORTEX. *Mon. Wea. Rev.*, **127**, 1693–1705, Crossref.

____, G. R. Marion, and S. W. Nesbitt, 2017: The regulation of tornado intensity by updraft width. *J. Atmos. Sci.*, **74**, 4199–4211, Crossref.

Van Den Broeke, M. S., 2017: Polarimetric radar metrics related to tornado life cycles and intensity in supercell storms. *Mon. Wea. Rev.*, **145**, 3671–3686, Crossref.

____, 2020: A preliminary polarimetric radar comparison of pretornadic and nontornadic supercell storms. *Mon. Wea. Rev.*, **148**, 1567–1584, Crossref.

Wood, V. T., and R. A. Brown, 1997: Effects of radar sampling on single-Doppler velocity signatures of mesocyclones and tornadoes. *Wea. Forecasting*, **12**, 928–938, Crossref.

Wurman, J., K. Kosiba, T. White, and P. Robinson, 2021: Supercell tornadoes are much stronger and wider than damage-based ratings indicate. *Proc. Natl. Acad. Sci.*, **118**, 1–8, Crossref.